12-2020

Nondestructive Evaluation (NDE) of Additively Manufactured Metal (AMM) Parts Using Ultrasonic Testing (UT)

Austin M. Thomas

University of New Haven
TAGLIATELA COLLEGE OF ENGINEERING
MECHANICAL & INDUSTRIAL ENGINEERING DEPARTMENT

Nondestructive Evaluation (NDE) of Additively Manufactured Metal (AMM) Parts Using Ultrasonic Testing (UT)

A THESIS
submitted in partial fulfillment
of the requirements for the degree of
MASTER OF SCIENCE IN MECHANICAL ENGINEERING

BY

Austin M. Thomas

University of New Haven
West Haven, Connecticut

December 2020

Nondestructive Evaluation (NDE) of
Additively Manufactured Metal (AMM) Parts
Using Ultrasonic Testing (UT)

APPROVED BY

Eric A. Dieckman

Eric A. Dieckman, Ph.D.
Thesis Advisor

Maria-Isabel Carnasciali

Maria-Isabel Carnasciali, Ph.D.
Committee Member

G. Ravi

Ravi Gorthala, Ph.D.
Committee Member

Cheryl Li

Cheryl Li, Ph.D.
Program Coordinator

R S Harichandran

Ronald S. Harichandran, Ph.D., P.E.
Dean, Tagliatela College of Engineering

Mario T. Gaboury

Mario T. Gaboury, J.D., Ph.D.
Interim Provost

Acknowledgements

I would like to thank John Kelley and Mark Morton for their assistance in fabricating the experimental apparatus by sharing hardware and tips of the trade. Maria-Isabel Carnasciali provided much needed moral support and mentorship along the way. Lastly, I must thank Joe Gabriel from Form 3D Solutions LLC for his immense assistance in producing the additively manufactured specimens for this project.

Abstract

Additive manufacturing is a category of emerging manufacturing processes that have applications in creating metal components with high value and complexity. The adoption of these parts is limited by the lack of fully developed nondestructive techniques for identifying internal defects. The use of ultrasonic testing for detecting and measuring internal features in additively manufactured metal parts is investigated. A low-cost ultrasonic immersion testing system was designed, constructed, and validated for the inspection of an additively manufactured titanium specimen with artificial defects as well as other metal artifacts. An ultrasound calibration block was additively manufactured from stainless steel type 316L and directly compared to a conventionally produced AISI 1018 steel block using standard inspection techniques. It was found that additively manufactured stainless steel has noticeable acoustic anisotropy with its speeds of sound varying nominally by 8% and greater attenuation than 1018 steel by a factor of at least $0.2\frac{\mathrm{Np}}{\mathrm{in}}$. To accompany experimental results, elastic wave simulations in a commercially available finite element package were explored.

Contents

List of Tables

List of Figures

Chapter 1

Introduction

1.1 Additive Manufacturing of Metal

Additive Manufacturing (AM) is a category of manufacturing processes by which objects are built from raw material layer-by-layer according to 3D model data. AM has gained traction in industry during the last 30 years as a rapid prototyping method as well as a means of low volume commercial production of intricate and customizable parts [1]. While AM was first conceived for polymers, processes for fabricating Additively Manufactured Metal (AMM) parts from engineering alloys have since emerged. These processes enable the production of structural components for applications including aerospace systems with considerable cost and weight reductions compared to conventionally produced parts [2]. Components with high value and complexity such as biomedical implants can be produced by AM in a single step rather than requiring the fabrication of a mold or various machining and/or assembly operations [3].

AM processes for metals can generally be categorized as Powder Bed Fusion (PBF), in which powdered material in a chamber is fused into layers by an energy source, or Directed Energy Deposition (DED) in which material is fed into the energy source incrementally in powder or wire form [4]. Typical PBF AM processes for creating complex engineering-grade metal components include Electron Beam Melting (EBM) and Selective Laser Melting (SLM). Creating components from expensive and difficult-to-machine alloys like titanium or nickel, for instance, is made easier by AM processes since the raw material is sintered or

melted rather than cut and only the exact amount of material needed to build the part goes into the final product. Figure 1.1 shows a schematic of an SLM apparatus and an object being fabricated in this manner.

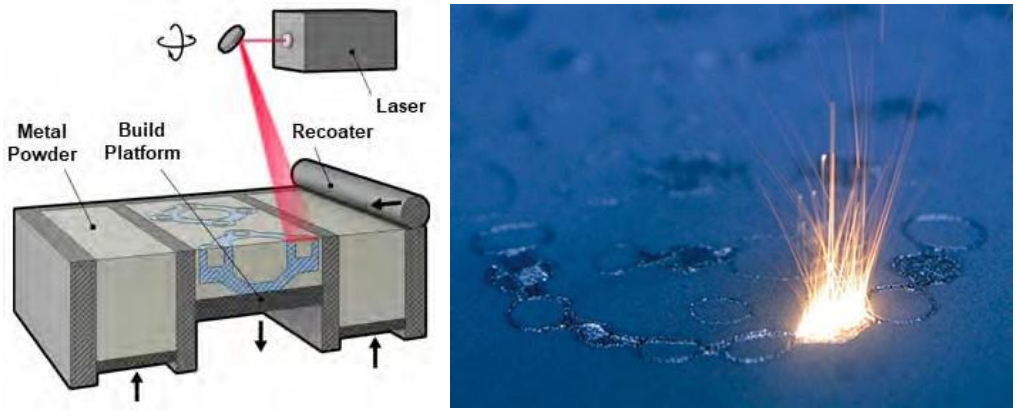

Figure 1.1: Schematic of an SLM process (1.1a) [5]. The apparatus uses a laser to fuse metal powder to a build platform. A recoater passes over the build after each layer to apply more powder. A part being made by SLM (1.1b) is surrounded by unmelted material while the laser scans over the top surface to fuse the successive layer [6].

1.2 Defects in AMM Parts

With any manufacturing process comes the challenge of verifying and controlling the quality of the product. Hidden flaws within a component can lead to premature failure, especially when under cyclic loading. While the flaws incurred by conventional manufacturing processes for metals such as welding and casting are well understood, there is a lack of research regarding the classification, prevention, and detection of flaws in additively manufactured metal parts. Defects that have been observed in AMM parts include porosity, lack-of-fusion, hot cracks, and delamination. These in particular are of interest as they can reside deep inside a part or just below the surface and cannot be detected visually.

Porosity is void space in the structure caused by a variety of factors including trapped gases in the powdered feedstock which create spherical pores in the final product. Process-

ing parameters such as scanning speed and power of the energy source can influence the development of various shapes and sizes of voids due to insufficient melt flow and/or particle ejection and evaporation [7,8]. Process-incurred voids, referred to as lack-of-fusion, can trap unmelted powder and are typically oblong and run perpendicular to the build direction. Pores and lack-of-fusion defects can concentrate stress and exacerbate crack growth, which has been shown to detrimentally reduce impact strength and fatigue life in titanium parts produced by SLM [9–11]. Examples of gas-induced porosity and lack-of-fusion defects are shown in Figure 1.2.

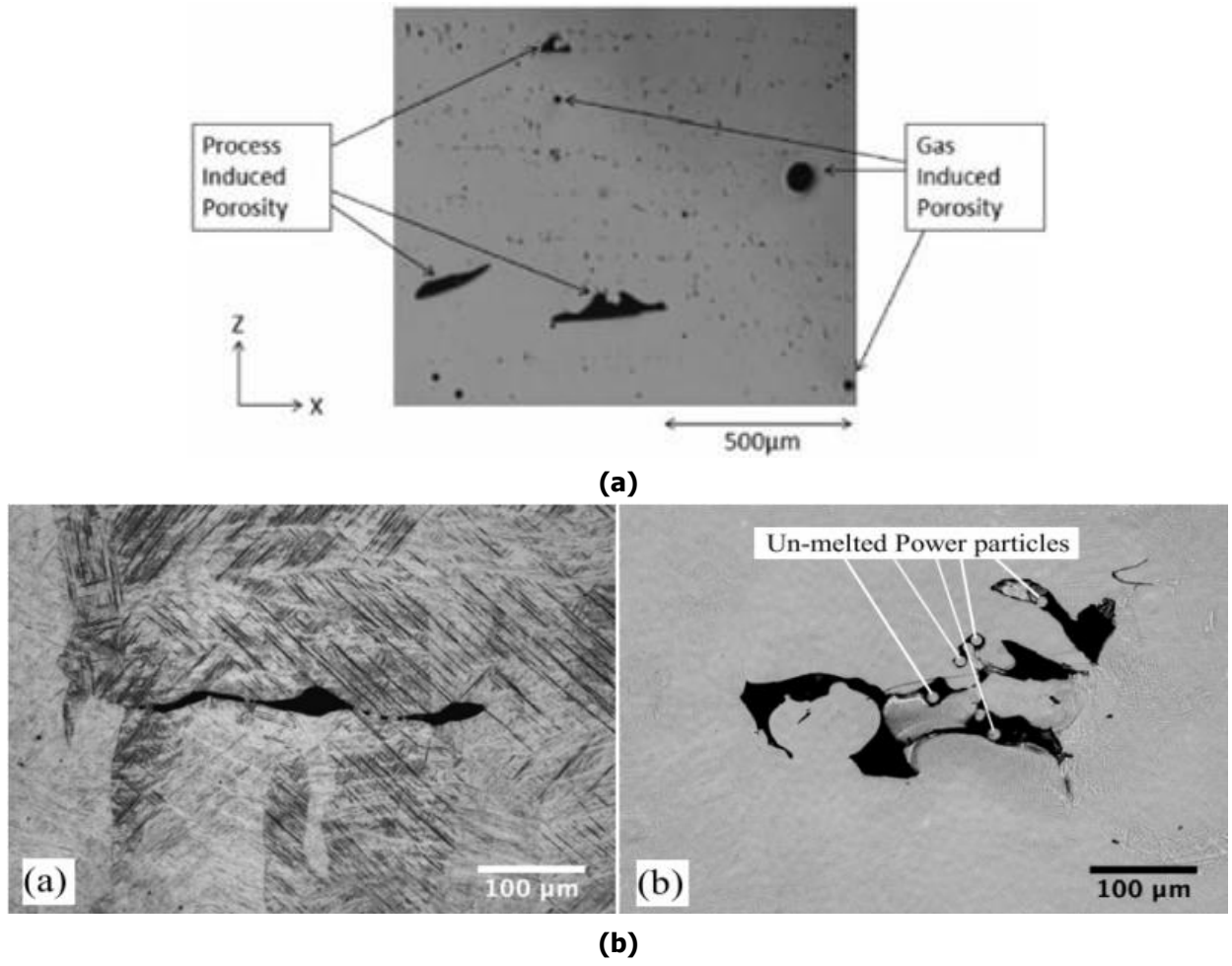

Figure 1.2: Porosity can arise in titanium produced by EBM (1.2a) due to gases trapped in the raw material and insufficient melt flow [7]. The same lack-of-fusion can be seem titanium produced by SLM (1.2b) and powder can become trapped in the voids [11].

Cracks can form and propagate both in the build direction of the part and along its layer interfaces. Vertical hot cracks in AMM parts have been found to form during the build due to incomplete fusion between recently molten metal and the surrounding material. When the energy source is passed over the structure too quickly or with too low power, the solid material surrounding the melt pool contracts when cooled and the liquid metal is too viscous to flow into the resulting void space before transitioning into solid form [12]. Figure 1.3 shows an example of hot cracking in an additively manufactured aluminum part. Residual thermal stresses in the material due to nonuniform thermal expansion and contraction can amplify vertical cracks as well as incur cracking along layer interfaces and even complete layer separation known as delamination [13]. Residual stress can also lead to geometric distortion that could render a part out of tolerance [14]. Even without cracks being present in the final product, the presence of residual stress in a part can reduce its load-carrying capability and lead to unexpected failure.

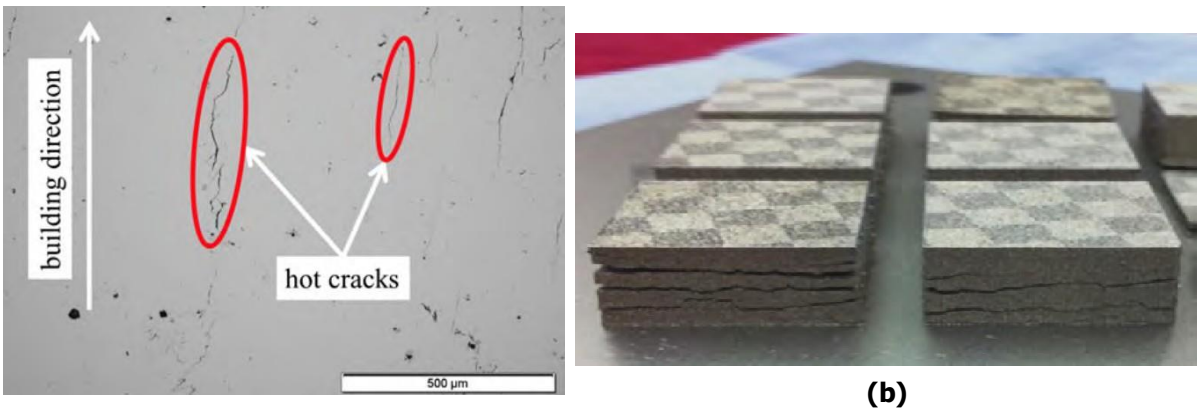

Figure 1.3: The SLM process can cause vertical hot cracks, as shown within a high strength aluminum part (1.3a) [12]. Horizontal thermal stress between layers during this process can lead to delamination, demonstrated in tool steel (1.3b) [13].

The aforementioned defects may be mitigated or prevented by modifying process parameters such as power density, scanning speed, and base plate temperature [15–17]. Post-processing treatments are in development to seal pores and homogenize the microstructure of certain alloys [18]. Spherical gas pores in AMM parts are typically smaller than 100µm

in diameter and not thought to be as worrisome as acicular lack-of-fusion voids greater than $200\mu m$ in length when it comes to undermining the fatigue strength of the material [19]. While the research relating to the effect of process parameters on the level of porosity and strength of bulk AMM structures is quite extensive, less work has been done to study the characterization and detection of failure-inducing defects.

1.3 NDE Challenges for AMM

Nondestructive Evaluation (NDE) is the practice of inspecting a manufactured part or assembly for critical defects while maintaining its usability. NDE is often the last stage of inspection before a component is certified to be used and may be performed during the manufacturing process or on a periodic basis after the it has been put into service. The NDE methods currently used in industry for metal parts are optimized for detecting well-understood flaws resulting from conventional manufacturing processes and not for those that are found in AM. Additionally, there is a lack of data relating the type, size, and location of a defect to the structural properties of an AMM part, so it is unclear what constitutes a critical defect [20]. Without this understanding, there is the possibility that a catastrophic flaw could be missed by an inspection technique that was calibrated for conventional metal components and their characteristic defects. Much work is needed to develop standardized NDE procedures for AMM parts, including extensive research into the effect of raw material quality, machine type, processing parameters and post-processing treatments on the mechanical properties of the parts and collection of probability-of-detection data for various flaws. Also, the creation of physical reference standards such as gauge blocks with known dimensions and defects is essential for the calibration of any new technique. In 2018, ANSI published a roadmap for standardization of AMM part production highlighting various knowledge gaps [21]. Some notable gaps that were addressed are the lack of understanding of the application of NDE to parts produced by AM, the need for standards for the design and

manufacture of calibration artifacts to demonstrate detection of naturally occurring flaws, and the need for an industry standard that establishes NDE acceptance classes for fracture critical AM parts.

Existing types of NDE methods for metals each present their own benefits and drawbacks when considering metal parts produced by AM. Visual Testing (VT) techniques including Penetrant Testing (PT) are optimized for detecting surface-breaking flaws. Airbus currently uses PT to inspect AMM parts in-line with their processes for inspecting cast parts [22]. This procedure is made more difficult by the inherent as-built surface roughness of AMM parts and simply cannot be used to detect sub-surface defects. Electromagnetic NDE methods such as Eddy Current Testing (ET) are applicable to electrically conductive materials but have limited depth of penetration, being best suited for shallow sub-surface defects. Radiographic Testing (RT) involves passing ionizing radiation through a component in search of voids, which allow more radiation through than solid material does. X-ray Computed Tomography (XCT) is an RT technique which is used primarily in the research context for achieving thorough 3D scans of metal parts (Figure 1.4). XCT is often employed as a way to corroborate the results of other destructive and nondestructive testing methods [20,23,24]. XCT can produce detailed visualizations and accurate measurements of internal and external

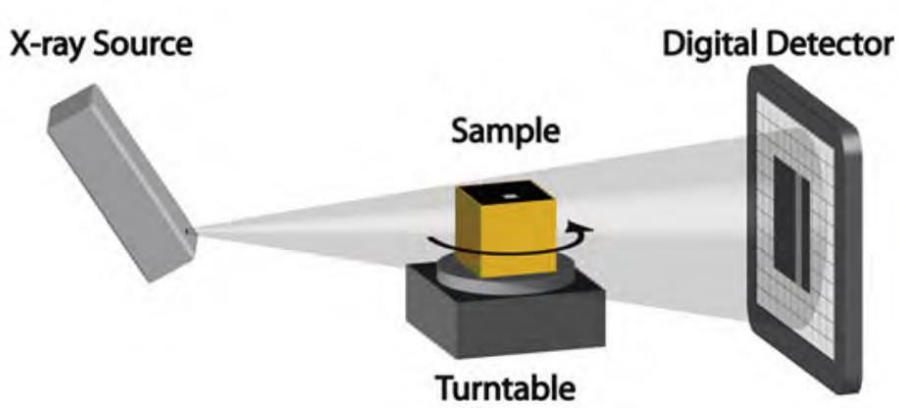

Figure 1.4: Schematic of X-ray computed tomography process [25]. Volumetric defects in a part allow more radiation to pass through and reach the detector. Scans are taken from many angles to fully image the geometry of the sample.

features but it has limited capability to detect cracks and has reduced sensitivity in large or thick parts. Other drawbacks include requiring expensive equipment in a specialized laboratory space and time-consuming data processing. Lastly, of the common NDE methods for metal components, Ultrasonic Testing (UT) is applicable to all metals, can be used to inspect deeply embedded features, and has relatively high sensitivity to defects of relevant size to incur failure. Figure 1.5 shows a chart comparing the applicability of various NDE methods to detecting defects in AMM parts.

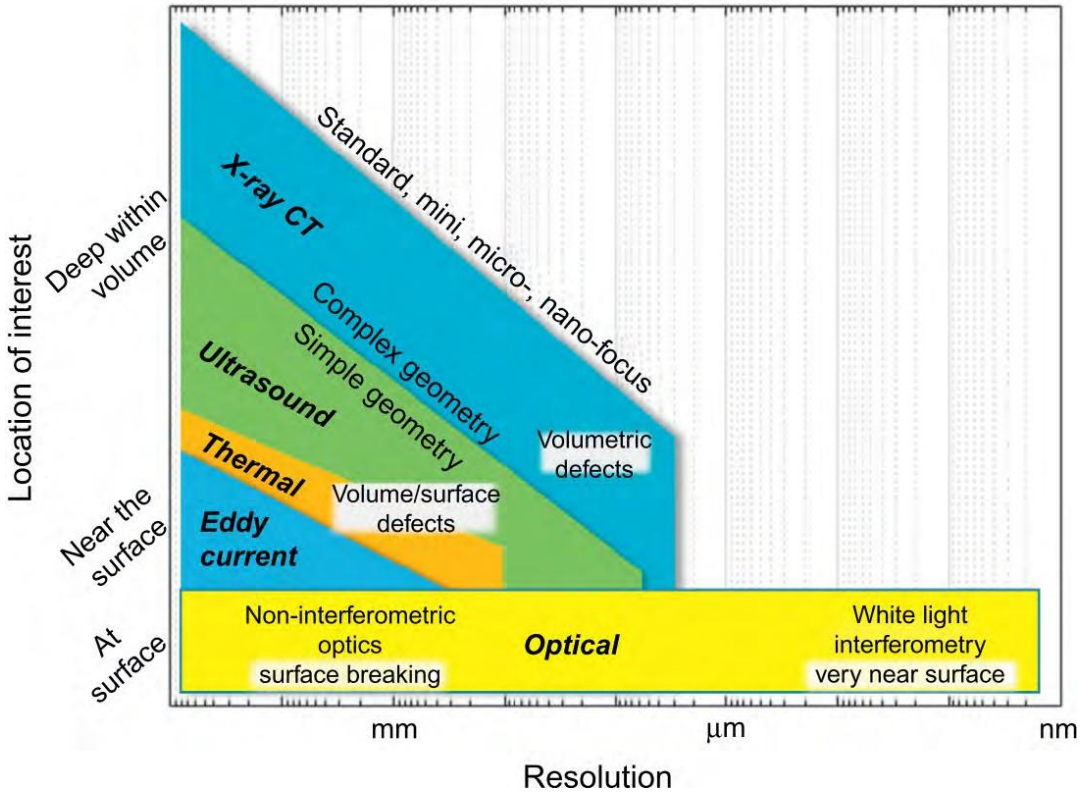

Figure 1.5: Comparison of NDE methods for AMM parts [26]. Optical methods have the finest resolution but are limited to the surface. Electromagnetic and thermal techniques are most applicable for larger defects near the surface. UT and XCT have the deepest penetration but have higher resolution near the surface. XCT is best used for detecting voids in complex geometries while UT can detect various defects in simpler parts.

Industry Standards

Companies and research organization around the world are in the process of developing recommendations and procedures for designing, fabricating, testing, and qualifying AMM parts. In 2013, NIST published recommendations and plans for standardization [27]. Among the priorities addressed are the evaluation of existing NDE techniques for use on AMM parts and development of new methods for in-situ and post-process NDE. ASTM has a committee on AM technologies which has published standards for measuring the mechanical properties of AMM parts and for assessing the feedstock materials for metal AM [28,29]. This committee is currently working on standards related to orientation and location dependence of mechanical properties for AMM parts and nondestructive testing for use in DED AM processes [30,31]. ASTM's subcommittee on specialized NDT methods recently published a guide for NDE of AMM aerospace parts after build [32]. Additionally, ISO is working on a standard for nondestructive testing of additive manufactured products and a standard guideline for intentionally seeding flaws in parts [33, 34].

While NDE standards for AMM parts are in various stages of development, these parts are already being incorporated in various applications. NASA for instance requires all AMM parts to go through comprehensive volumetric and surface NDE regardless of their application. Additionally, parts with a high consequence of failure must meet the same criteria as those produced by conventional means [20]. Companies such as Lockheed Martin have their own internal procedures for qualifying additively manufactured parts and generally rely on current industry norms to verify the quality of suppliers' procedures and facilities for producing them [35]. The widespread adoption of AMM components in high-stress applications is still limited due in part to the lack of standardization tracing all the way back to the raw material production. As information about mechanical properties, defects, and NDE techniques regarding AMM parts becomes more broadly available, more organizations may implement these parts rather than relying on their own proprietary data and protocol.

1.4 Ultrasonic Testing

Ultrasonic Testing (UT) is a category of NDE techniques that involve sending sound waves through a material via an ultrasonic probe and recording the time and amplitude of their reflections to identify internal discontinuities (Figure 1.6). UT is useful for the detection of deep internal defects including cracks and can be deployed in a portable manner for in-service inspections. The simplest data set that can be acquired with ultrasound is

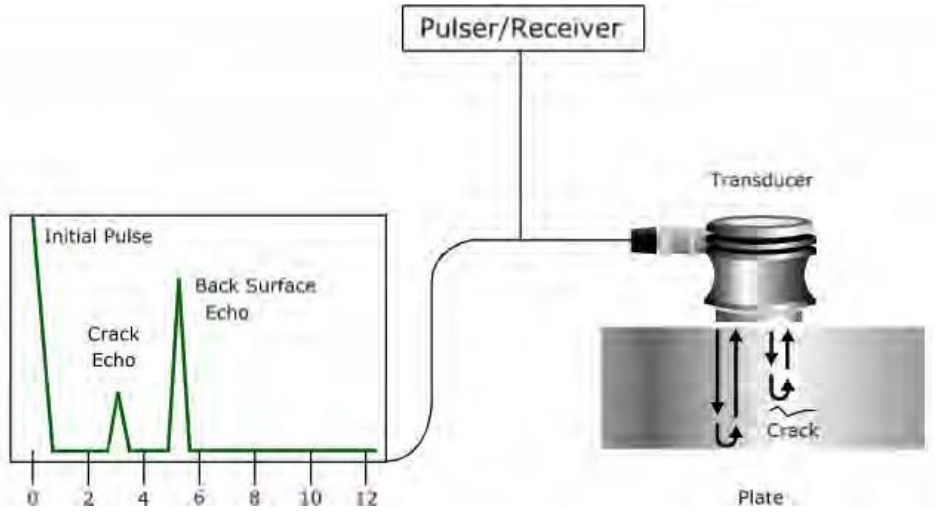

Figure 1.6: Schematic of ultrasonic testing process [36]. A transducer sends acoustic energy through a sample, and the reflections from the backwall and any discontinuities are plotted on an amplitude versus time graph, known as an A-scan.

an amplitude versus time plot representing the reflected acoustic energy at different depths within the sample taken at a single probe location, or an A-scan. By translating a probe along a line and collecting A-scan data at multiple points, a B-scan can be constructed, which represents a side view of the test sample (Figure 1.7). By collecting A-scan data at several points in a 2D grid, a C-scan can be constructed, which can be interpreted as a top view of the component with colors used to represent variations in thickness (Figure 1.8).

Piezoelectric ultrasonic probes are generally categorized as single-element or phased array. While a single transducer can only inspect a small region, using a compact array of transducers, or Phased Array Ultrasonic Testing (PAUT), enables the capability for perform-

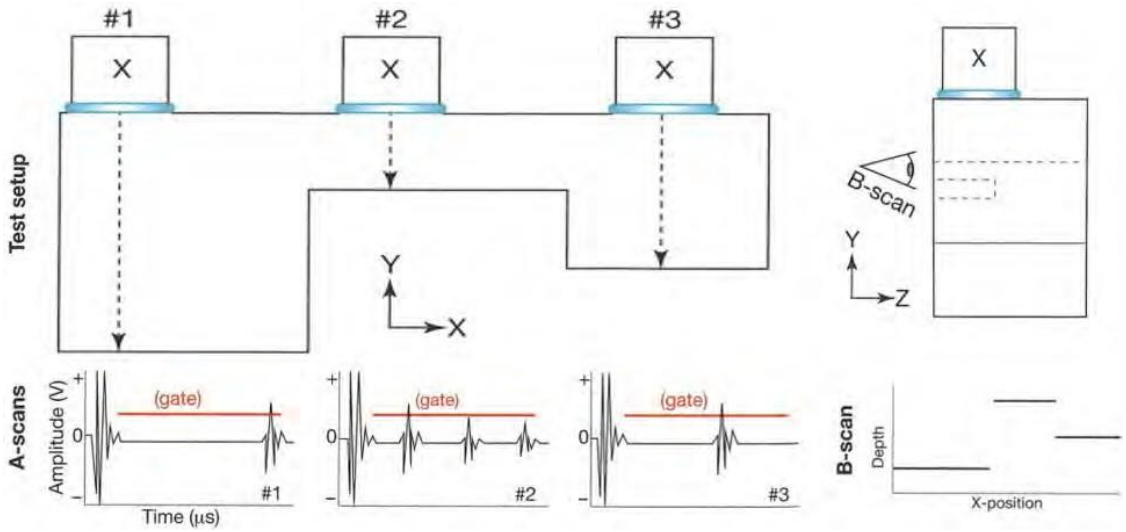

Figure 1.7: Schematic of A-scans being compiled into a B-scan [37].

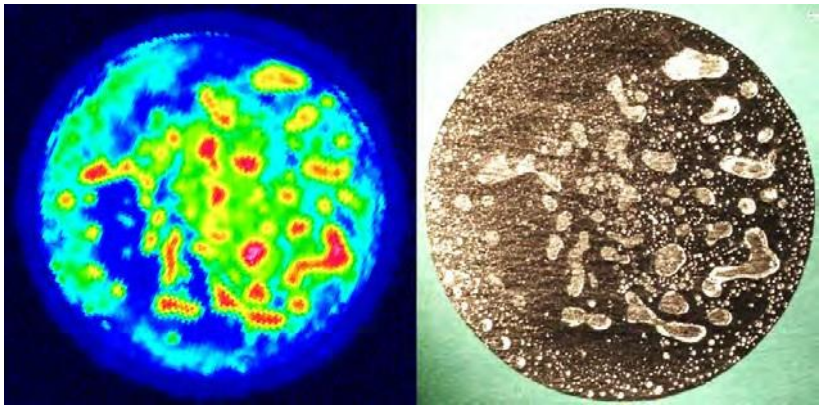

Figure 1.8: Example of a C-scan of a brazed joint [38].

ing more complex measurements across a larger area at one instant. By varying the times at which the elements pulse and receive signals, PAUT can be applied to uneven or curved surfaces and sweep across multiple frequencies in a single inspection. Another UT method is angle beam inspection, in which the probe—either single-element or phased array—is mounted to an angled wedge that acoustically couples to the surface of the test specimen. This configuration allows the examination of features that are not accessible overhead. Using a phased array probe in an angle beam inspection can yield a sector scan, illustrated by Figure 1.9, which is essentially multiple A-scans at different angles stitched together.

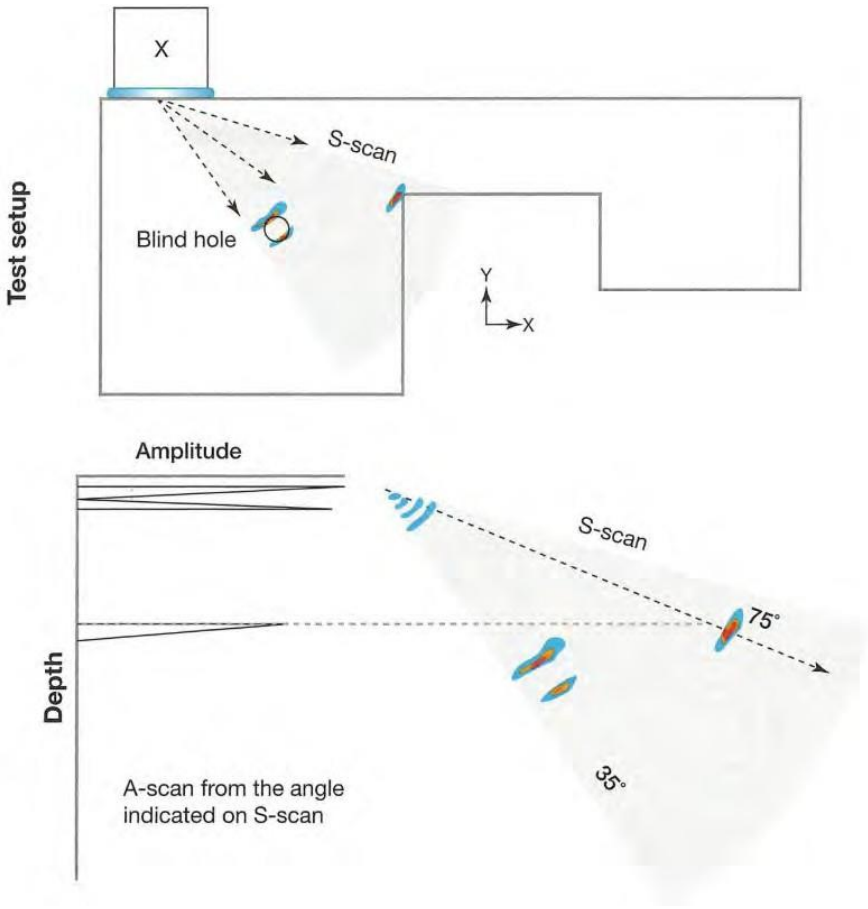

Figure 1.9: Schematic of a sector scan [37].

One drawback of UT is that when performed by hand, inspections are limited to a small area and the positioning of the probe is not very repeatable. Also, when inspecting a metal component, liquid couplant must be consistently applied to the surface to ensure effective transmission of sound energy between the probe and the part. One method to overcome this challenge is immersion testing, wherein the component being inspected is submerged in water—which acts as a couplant—while the probe movement is automated. Figure 1.10 shows a schematic of an immersion testing apparatus. The benefit of this technique is that since the water constantly surrounds the specimen, the probe does not have the potential to lose coupling with the surface. Using such an automated apparatus enables greater repeatability when scanning multiple of the same component compared to having a technician follow

a procedure by hand. Immersion testing systems can be equipped with several degrees of freedom so that the probe can always be oriented normal to the surface of the test specimen, making it applicable to inspecting curved geometries.

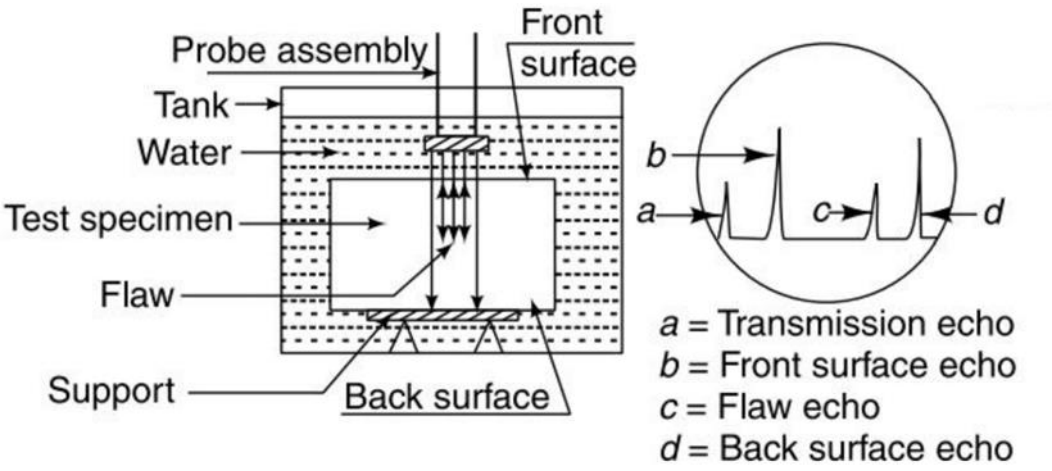

Figure 1.10: Schematic of an immersion testing apparatus and the resulting signal [39].

Research on UT of AMM Parts

While ultrasonic testing is a mature area of NDE when applied to conventionally fabricated metal components, it has not been applied as widely to AMM specimens in part because of the different acoustic properties of their material structure. Parts produced by AM processes have been found to have directional anisotropy in their mechanical properties, often marked by lower tensile strength and stiffness in the direction transverse to the layers [40]. The microstructure of AMM parts produced by PBF processes consists of columnar grains running vertically in the build direction and skewed to follow the scanning pattern of the energy source during fabrication. It has been shown that this grain structure leads to acoustic anisotropy. For instance, in aluminum specimens produced by AM, the longitudinal wave speeds in each principal direction are virtually identical, but shear waves oscillating in the plane of the build layers propagate slower than other shear waves by a factor of 0.8% [41]. Stainless steel specimens produced by SLM have also been found to have a greater speed of

sound in the build direction compared to along the layers [42]. The sound speeds are also impacted by heat treatment, which alters the bulk density of the part.

The internal structure of AMM parts is typically more attenuative to sound waves than conventionally produced metals. High anisotropy can lead to high attenuation and noise which could mask defects. This attenuation has been measured for 17-4 PH stainless steel and found to generally increase with grain size [43]. New focusing techniques are in development to improve the signal-to-noise ratio and resolution for such high attenuation and scattering materials and have been demonstrated on titanium specimens [44]. Nonlinear ultrasound techniques have been investigated and shown to be effective for characterizing artificial defects and porosity within titanium specimens produced via EBM [45]. Statistical methods have also proven useful in distinguishing flaw echoes from structural background noise when inspecting porosity in SLM 316L stainless steel [42].

Additively manufactured metal components typically have rough and wavy surfaces that can pose a challenge for UT. Additionally, intricate features that are advantageous to fabricate with AM can be difficult to inspect. Recent advances in focusing algorithms and the use of flexible transducer arrays to inspect anisotropic welds and complex features are promising when considering their application to AMM parts [46,47]. More recently, the effect of surface waviness on flaw detection capability has been investigated for aluminum specimens made using a wire arc AM method [48]. A desirable innovation in the area of metal additive manufacturing is the development of in-situ process monitoring technology. UT has been explored in this area by embedding ultrasonic probes into the build platform to measure variations in sound speed [49] but thus far no NDE method has been implemented commercially into a metal AM machine.

An area that remains relatively unexplored in the context of AMM parts is the characterization of lack-of-fusion defects using ultrasound. Porosity has been an area of interest in many studies, ranging from XCT measurements to destructive and fatigue testing. Lack-of

fusion defects tend to be thin and narrow and often contain loose unconsolidated powder, as opposed to pores which are typically round. Both can be detrimental to a part's fatigue strength due to stress concentration. The influence of unconsolidated powder on the probability of detecting the defect using ultrasound has not been fully investigated. Additionally, as of yet there are no official calibration standards for metals produced by additive manufacturing. Such a reference artifact is crucial for performing UT inspections as it has precisely known dimensions and geometric features that are used for quantitative measurements of speed of sound as well as qualitative comparisons between flawed and flawless areas. Many calibration standards exist for inspecting conventionally produced metals, yet thus far in the literature there is no published use of one of these artifacts produced by AM. While it is clear that there are differences between additively manufactured and forged or cast metal parts in their mechanical properties, it has not been explored whether it is necessary to design completely new artifacts in order to calibrate UT equipment for inspecting AMM parts.

Chapter 2

Immersion Tank Build

An ultrasonic immersion system is desirable for performing automated and high-resolution inspections of components of various sizes, shapes, and materials. Such systems typically cost several thousands of dollars at the minimum and require a large amount of floor space in a laboratory environment. To further the ultrasonic testing research efforts at University of New Haven, an immersion tank was custom built for under $1000 to interface with existing ultrasound hardware. The immersion testing system was validated by performing inspections of metal artifacts including a titanium blocked with artificial internal defects fabricated via SLM.

2.1 Design

A repurposed 75 gallon aquarium tank was selected as the basis of the immersion testing apparatus. Using open-source linear motion hardware, a two-axis gantry was designed to make optimal use of the size of the tank, resulting in an effective scanning area of approximately $1000 \times 300\text{mm}$. The intended use for the system was to acquire C-scans of components with planar top-surface geometry, so there was no need to automate the vertical movement of the probe. The desired probe can be mounted to an aluminum tube, which the operator adjusts to bring closer to the top surface of the test specimen and secures with a clamp. By limiting the degrees of freedom of the mechanism to two which are motorized and one which is adjusted manually, the complexity and thus cost of the system was kept low. The modular nature of the linear motion hardware presents the option to add a motorized

z-axis actuator or rotational axis if that is desired in the future. A rendering of the apparatus is shown in Figure 2.1a. The immersion tank was designed to interface with the GE Mentor UT inspection system which was already in use for research at University of New Haven. The Mentor, shown in Figure 2.1b, has a user interface with built-in applications for various common field inspections.

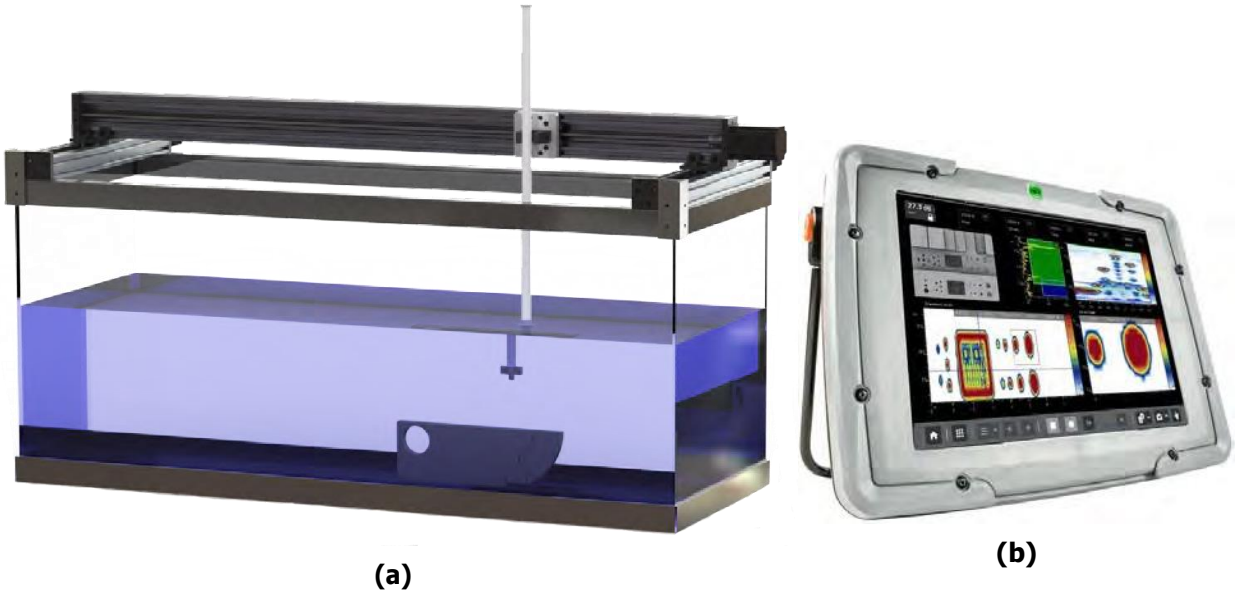

(a) (b)

Figure 2.1: Rendering of immersion tank apparatus (2.1a) and GE Mentor UT (2.1b).

The gantry of the scanner is driven by stepper motors and lead screws, enabling smooth and precise motion with positioning resolution of 0.04mm. To drive the motors, an Arduino MEGA 2560 microcontroller and Wantai DQ542MA stepper motor drivers were chosen. Using an open-source microcontroller was essential for complete customization of the operation of the apparatus. The signal flow for the entire system starts in a user interface created in MATLAB where the desired position or scan parameters are entered by the operator and transmitted over USB to the microcontroller which commands the motors to move the ultrasonic probe. Figure 2.2 illustrates the signal flow of the immersion testing system. One limitation of using the Mentor system is the inability to directly trigger it to send pulses to the transducer and thus collect data. The only supported input is a single rotary encoder

which, when mounted to roll along the x-axis actuator, sends a signal to indicate the relative position of the probe in that axis to the nearest 0.06mm. To construct B-scans and C-scans, the Mentor must be running an application for encoded scanning in which it is set up to pulse and receive A-scan data whenever the probe moves by a given distance as it translates the width of the scan area.

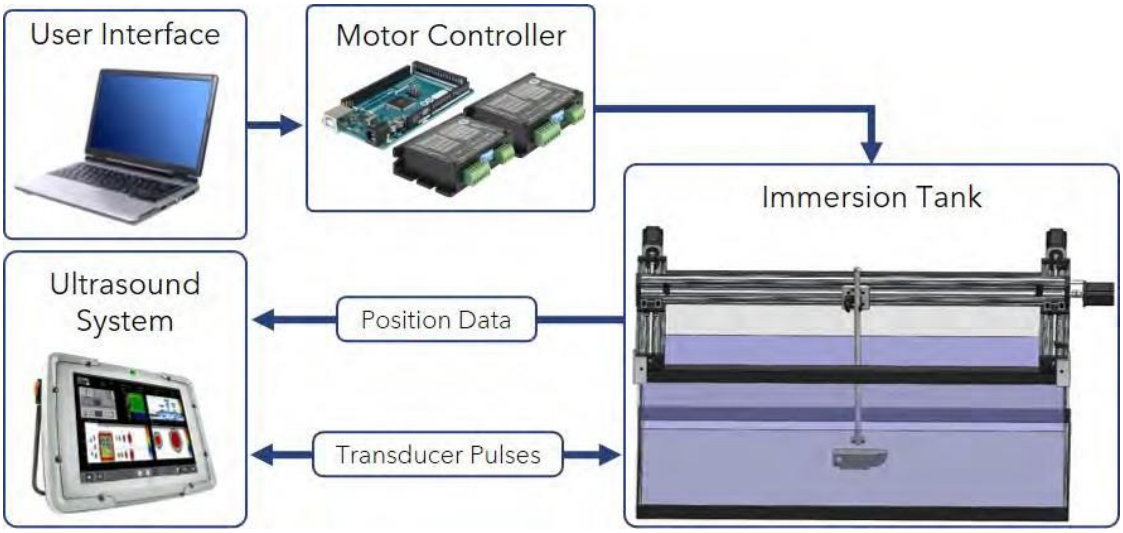

Figure 2.2: Signal flow schematic for immersion testing system.

The graphical user interface for the immersion testing system shown by 2.3, was created in MATLAB using the GUIDE environment. In this interface, the user sends simple motion commands to the scanner by selecting the axis, direction, distance, and speed to move. By entering these parameters and pressing the "Jog" button, a string is communicated to the microcontroller over USB, which parses the data and commands the desired axis to move using a custom *MotorMove* function. The full Arduino code is included in Appendix A. Both the user interface design and structure of the motion control code were based on work done by Souissi and Dieckman on an ultrasonic pipe delamination detector in 2019 [50]. The detector and this immersion system use similar electronics, which are all housed in a central enclosure that was custom designed and fabricated. The entire experimental setup for the immersion testing system is shown in Figure 2.4.

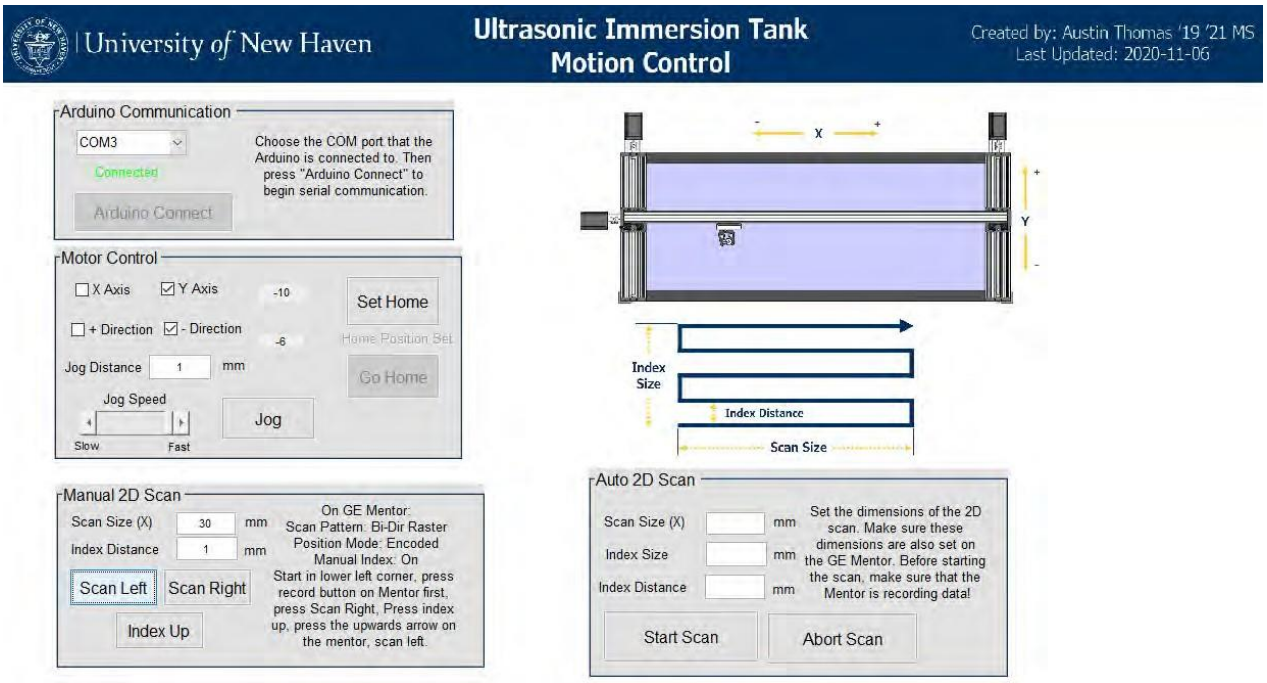

Figure 2.3: User interface for immersion testing system.

Since the 2D scanning applications loaded on the GE Mentor do not readily accommodate more than one encoder input, the y-axis of the scanner must be indexed by the operator. To perform a scan, the scan size (x), index size (y), and index distance (y increment) are set on the Mentor and data recording is initiated. After using the jog controls to move the probe to the lower left corner of the scan area, the operator enters the scan size in the MATLAB GUI and selects "Scan Right," which commands the probe to be moved along the x-axis. The Mentor collects A-scan data along this path, constructs a B-scan from it, and plots the first row of a C-scan. The operator then selects "Index Up," and indicates on the Mentor that the row is completed. To scan another row, the user selects "Scan Left," and the process repeats until the entire area has been scanned. This process is rather slow for scanning large areas, especially when a single-element probe is being used. Further investigation into the GE Mentor's user interface or the adoption of a different ultrasound inspection system would hopefully enable fully automated 2D scanning, a feature that has been implemented into both the MATLAB GUI and Arduino code.

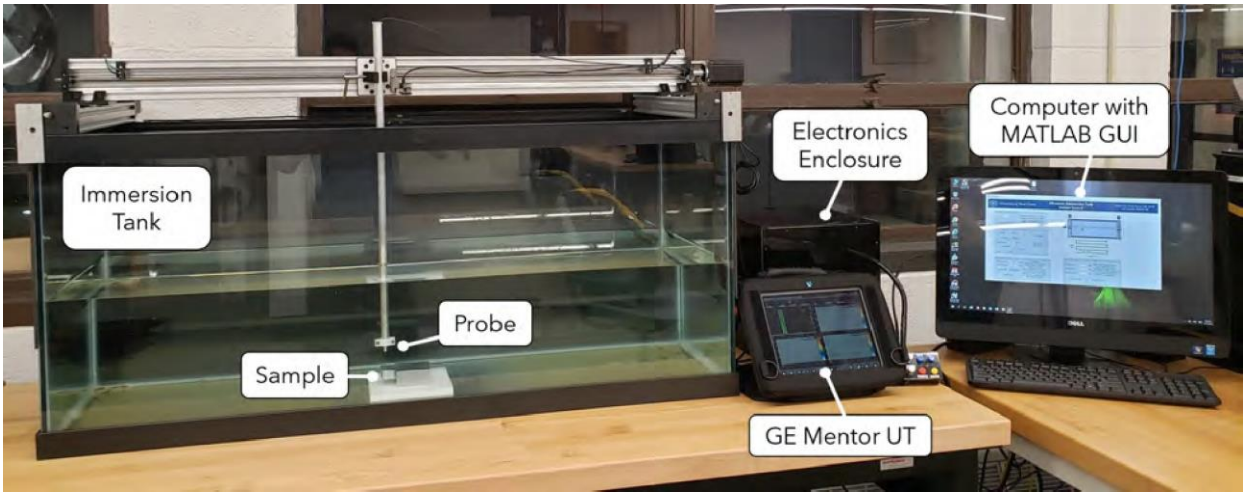

Figure 2.4: Experimental setup for immersion testing. A computer runs the user interface, which communicates to a microcontroller and motor drivers housed in an enclosure. The probe's position in the immersion tank in measured by an encoder that is connected to the GE Mentor ultrasound system.

2.2 Validation

To test the immersion testing system, several artifacts were inspected to produce sample B-scans and C-scans. As a precursor to this project, a specimen was fabricated from a titanium alloy containing artificial defects (Figure 2.5). The defects were designed to be elliptical in profile and to run longitudinally down the part in the direction of build. The ellipse shape was chosen to trap unconsolidated powder and mimic the oblong nature of lack-of-fusion defects. Each defect has the same major length; however, in one section, three defects with different minor lengths were placed with their major axes at the same distance from the inspection surface. In another section, four defects with the same dimensions were placed at different depths from the scanning surface. The specimen also includes a cutout to enable a two-point calibration of for speed of sound at 0.5" and 1" thicknesses. Figure 2.6 shows a B-scan of the titanium block taken along the center line using the immersion system with a 10MHz single-element unfocused transducer. The artificial defects are clearly visible at their respective depths. Without further analysis, it is difficult to resolve the

differences between the three defects with the same centerline depth. Since their thicknesses are 0.015", 0.01", and 0.005", the reflection of the thinnest defect should be detected 0.005" lower than that of the thickest one. The difference in thickness between these features is not easily measured using pulse-echo inspection, as a vast majority of the acoustic energy is reflected by the top of the defect. Even though these defects are filled with titanium powder, they reflect—rather than transmit—sound waves like a void would. Performing another inspection from the other side of the specimen would enable thickness measurements to be made. The GE Mentor UT unfortunately does not enable raw data output, so the numerical measurements must be read from the plots in the user interface.

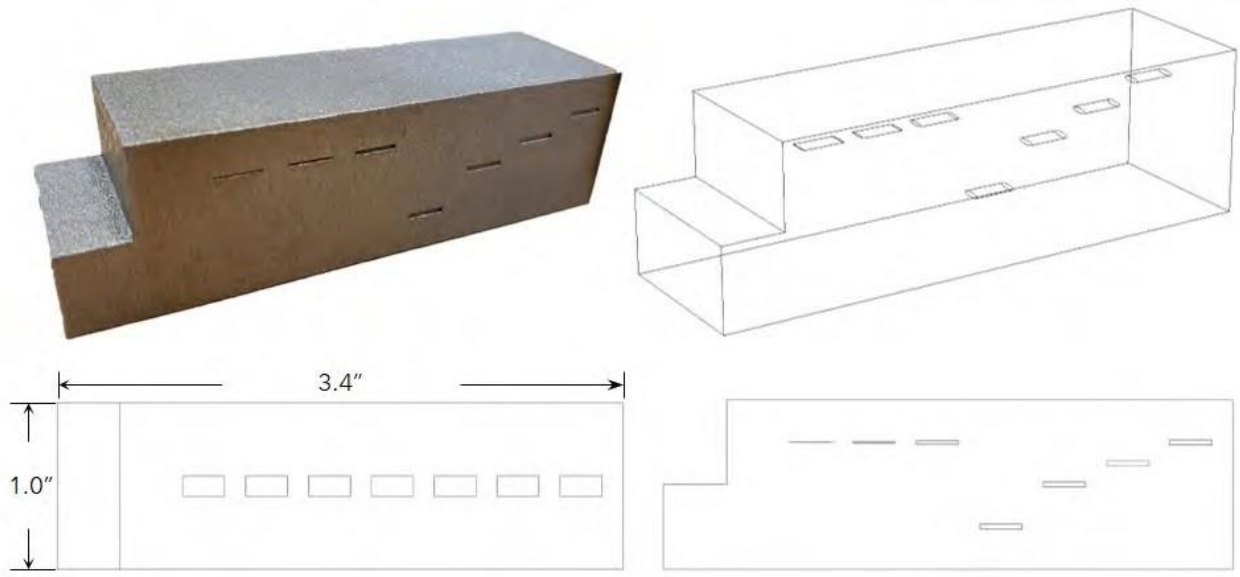

Figure 2.5: Titanium specimen with simulated internal defects of various thickness and lengths.

A C-scan of the titanium block was taken with a resolution of 0.005" along the x-axis and 0.04 along the y-axis (Figure 2.7). The block was oriented with its planar surface facing the probe such that the top surface reflection signal was constant throughout the inspection. To construct the C-scan, the peak amplitude of the backside reflections were plotted at each probe location. The colors range from blue for the lowest amplitude and red for the highest on a normalized scale. Thinner areas or regions with a discontinuity are indicated by a higher

Figure 2.6: B-scan of additively manufactured titanium block with artificial defects. Side view from 3D model file is overlaid to show accuracy of flaw echo locations.

amplitude signal as the sound waves have a shorter path in the material and thus attenuate less. With the chosen resolution and display settings, the defects can easily be located in the *xy* plane. It is difficult to discern their depths with this particular color scale, which is why a B-scan was also taken.

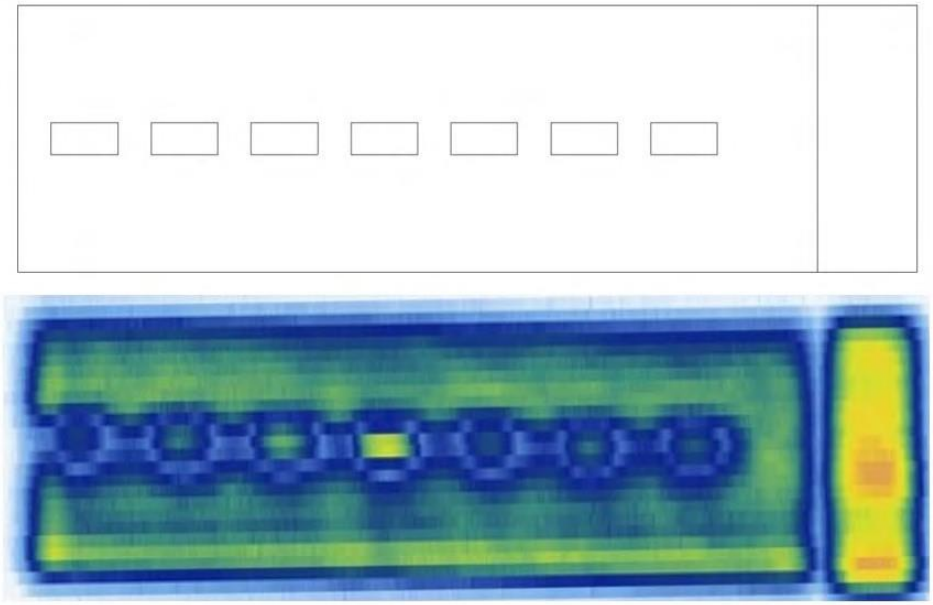

Figure 2.7: C-scan of additively manufactured titanium block.

In immersion testing, having the probe too close or far away from the sample can be detrimental to the resulting signal. The general rule for setting probe's location or the water path *WP* is given by Equation 2.1a in terms of the focal length *F*, longitudinal speeds

of sound in water c_{water} and the sample material c_{sample}, and the material path MP or sample thickness [42]. For an unfocused transducer, Equation 2.1b is used. With the custom immersion system, the operator refers to the A-scan readout on the ultrasound interface to adjust the distance between the probe and the sample. If the water path is too long, then the reflected signals from the sample are highly attenuated and difficult to discern. If the probe is too close to the sample, then the echoed reflections from the top surface and the inherent noise in the probe overlaps the signals from the backside and flaw reflections, thus obscuring them. Another consideration that must be made when performing an immersion test is to ensure parallelism between the top surface of the sample and the plane of the gantry. If the sample sits at a slight angle with respect to the path of the probe, the backside reflection may artificially vary across the part. To mitigate this, the metal specimen should be placed on a surface with a high impedance difference such as plastic with shims placed in between as necessary. Placing the sample onto a dissimilar material is crucial for ensuring a high proportion of incoming acoustic energy reflects off the back wall and returns to the probe.

$$WP = F - \frac{c_{water}}{c_{sample}} MP \tag{2.1a}$$

$$WP = \frac{c_{water}}{c_{sample}} MP \tag{2.1b}$$

To test the system's ability to detect fine details, a quarter coin was scanned with the same resolution as the titanium block using a spherically focused 10MHz transducer with a 2" focal length. A shortcoming of this system is that the y-axis resolution is limited by the Mentor's user interface to 1mm or 0.04" despite the gantry's ability to reliably position itself to the nearest 0.04mm and the rotary encoder being able to measure position to the nearest 0.06mm. Because of this limitation, the C-scans appear rather coarse. Figure 2.8 shows the setup and resulting scan of the obverse side of a quarter as measured through the thickness of the coin. A gate was set on the Mentor interface to surround the backside reflection,

and the peak amplitude in the gate was plotted at each probe location. Red areas indicate higher amplitude or sooner reflections in thinner areas of the coin. The general outline of Washington's head can be seen in the scan with not much more detail being distinguishable. Using a different ultrasound system that enables finer spatial resolution would enable finer scans to be taken. The ability to export numerical data for further analysis would also result in more meaningful scans.

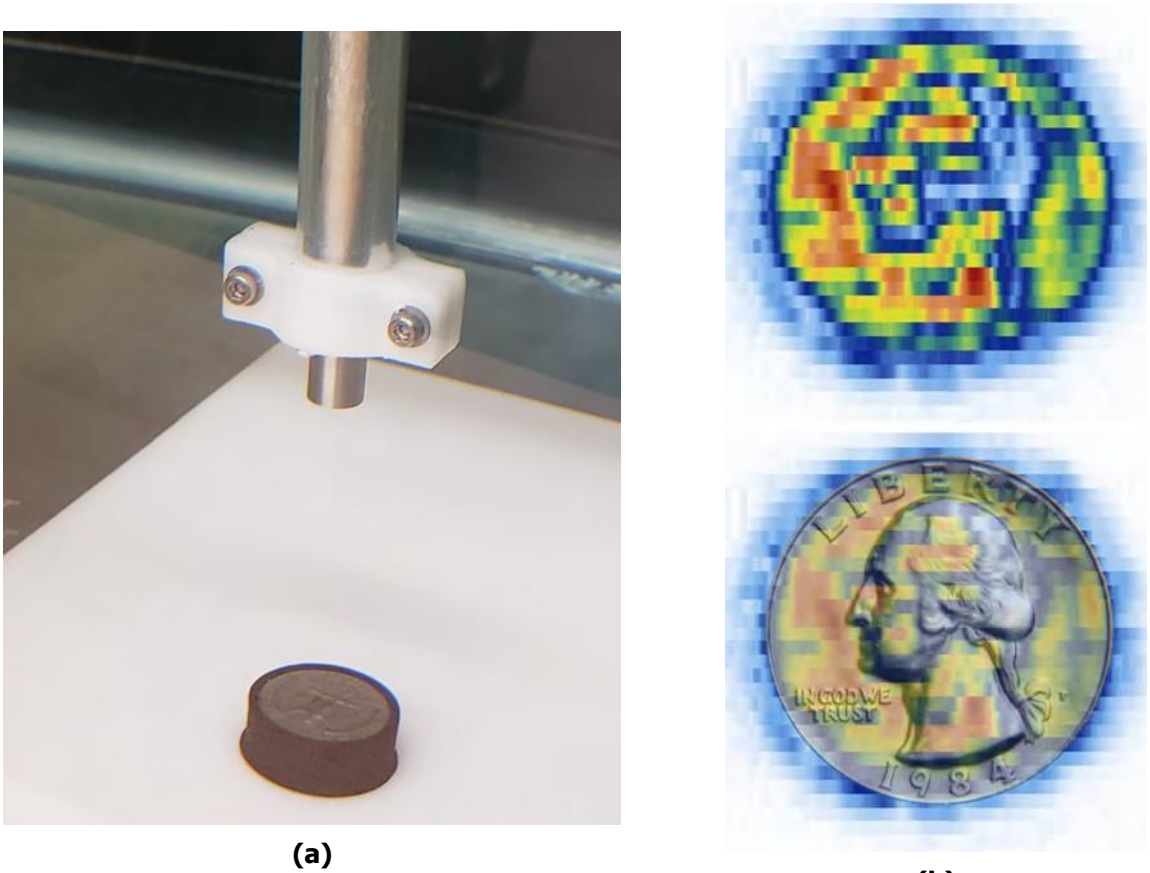

(a) **(b)**

Figure 2.8: Setup for immersion testing a quarter (2.8a) and resulting C-scan (2.8b).

Chapter 3

Additively Manufactured Ultrasound Calibration Block

In order to use ultrasonic testing to measure internal features in a given piece of material, it is necessary to know the acoustic properties of said material and to have a point of reference as to what a critical defect would look like as an acoustic signal. UT calibration standards do not currently exist for additively manufactured metal parts, as their microstructure is unique and their properties are anisotropic. The acoustic and elastic properties of these parts which are of interest for UT must be determined experimentally for each alloy and fabrication method used in AM. To investigate the need for a unique reference artifact for AMM parts, a mini IIW-2 calibration block was fabricated to compare to an existing one made from AISI 1018 steel. Measurements were taken of principal longitudinal and shear wave speeds and qualitative comparisons were made between inspections of notable geometry on the two blocks.

3.1 Test Specimen

An IIW-Type 2 block is a standard UT calibration artifact with various precisely known thicknesses and features [51]. The mini IIW-2 block developed by PH Tool is a more compact block with overall dimensions of 1”x 2”x 6”. The block’s features were measured and modeled in CAD such that it could be additively manufactured. The AM block was produced in stainless steel type 316L by Form 3D Solutions & Manufacturing on an EOS M290 SLM

machine. Due to the high cost and limited size of AMM parts, fabricating a full size IIW-Type 2 block, at 12" long, would not have been realistic. Figure 3.1 shows the two blocks.

(a)

(b)

Figure 3.1: Mini IIW-2 block fabricated from AISI 1018 (3.1a) and produced from SS 316L by SLM (3.1b).

3.2 Measurement of Sound Speed and Elastic Properties

Ultrasonic testing is used to measure distances based on the time of flight of sound waves in a solid material. The two wave modes which are most applicable to UT are pressure, also known as longitudinal or compression, and shear, which propagate at different speeds. Figure 3.2 shows a diagram of a pressure wave refracting at an interface and converting into a pressure and shear wave in the new medium. When inspecting a component using ultrasound, one does not always have direct overhead access to a particular feature, so an

angled wedge can be used to send a refracted shear wave into the part. Regardless of whether a pressure wave or shear wave is used for inspection, its respective speed in the material must be known for the operator to accurately relate the time of a reflected signal to the depth of an arbitrary feature.

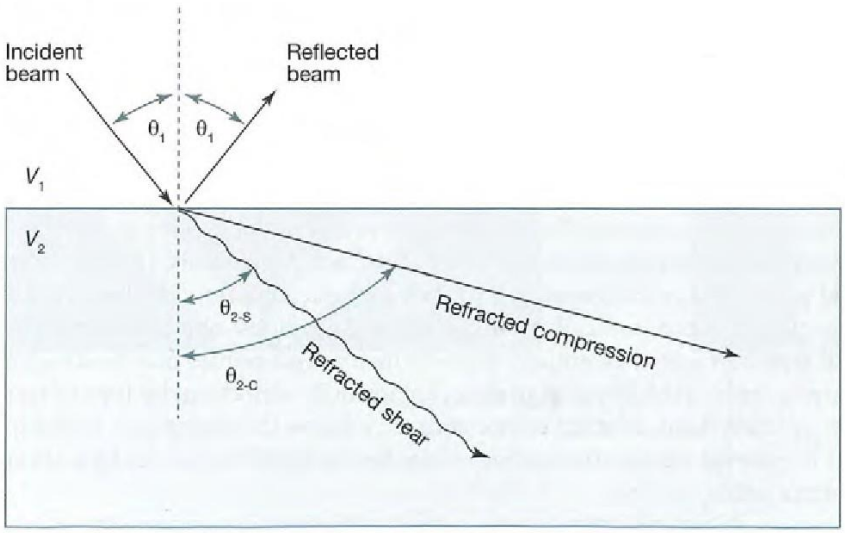

Figure 3.2: Diagram of refraction and mode conversion of sound waves at an interface [37].

The speeds of sound of a material can be measured experimentally using a pulse-echo ultrasonic inspection as long as the specimen has precisely known dimensions. A two-point calibration involves measuring the time of flight (TOF) of a sound wave through two different known thickness $d_{1,2}$ and computing the speed via Equation 3.1. The measured TOF is the round-trip time for a sound wave to propagate through the piece, reflect off the backwall, and return to the transducer, thus traveling twice the thickness.

$$c_{p,s} = \frac{2(d_2 - d_1)}{(\mathrm{TOF}_2 - \mathrm{TOF}_1)} \tag{3.1}$$

Figure 3.3 shows the setup for measuring longitudinal and transverse speeds of sound in the mini IIW-2 block. A straight single-element 2.25MHz probe was used to measure pressure wave speed through the 0.5", 0.75", and 1" thicknesses in the build direction of

the AMM part. Separate measurements were made along the layers using the 2" and 1.8" thick features of the block. A single-element 5MHz wedge probe was used to measure the shear wave speed, using the 1" and 2" radius arcs as calibration points. The measured sound speeds for the 1018 steel block and the additively manufactured 316L block are summarized in Table 3.1. There is noticeable acoustic anisotropy in the additively manufactured block,

(a)

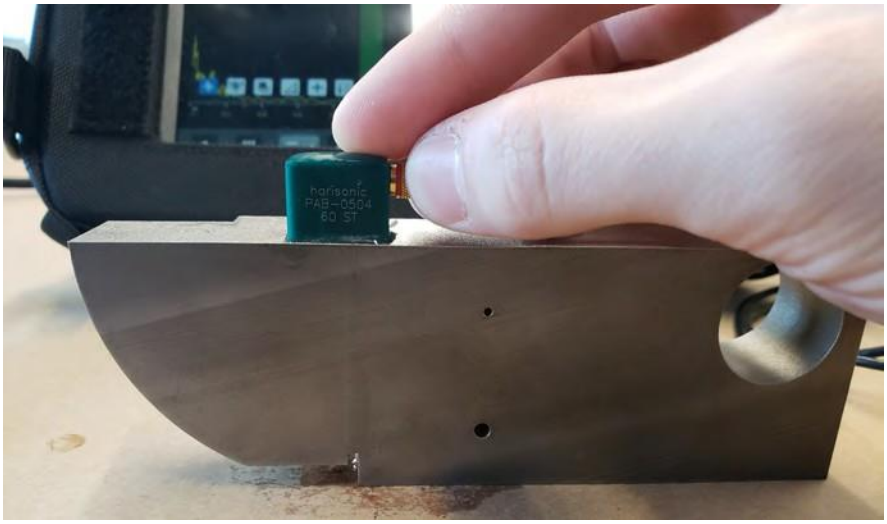

(b)

Figure 3.3: Using two-point calibration to measure pressure wave speed (3.3a) and shear wave speed (3.3b) in a mini IIW-2 calibration block.

Table 3.1: Measured speeds of sound in mini IIW-2 blocks

Material	$c_{p_{x,y}}$ [$in/\mu s$]	c_{p_z} [$in/\mu s$]	$c_{sx,y}$ [$in/\mu s$]
AISI 1018	0.233 ± 0.001	0.233 ± 0.001	0.127 ± 0.002
SLM SS 316L	0.227 ± 0.001	0.21 ± 0.01	0.120 ± 0.001

with the longitudinal speed of sound in the build direction being nominally 8% greater than the speed along the layers. Since the 1018 steel block is isotropic, its speed of sound is virtually identical in each direction. The uncertainty in these measurements was estimated using a 99% confidence interval based on a sample size of 10. The material coordinate system for an AMM part is illustrated in Figure 3.4, with z indicating the build direction and x and y running along the layers. Due to the design of the mini IIW-2 block, the shear wave speed in the xy plane could be measured, but not in the z direction.

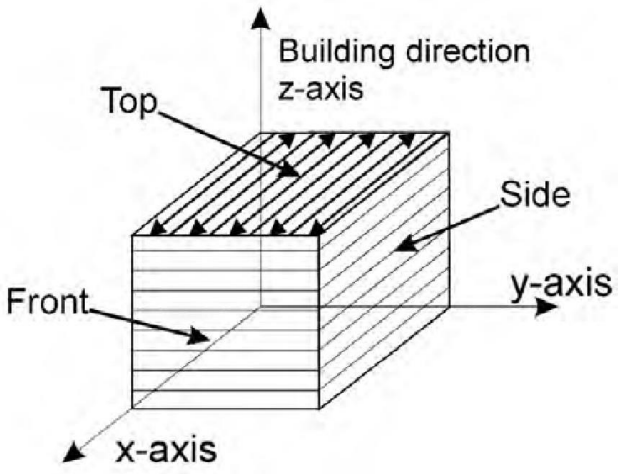

Figure 3.4: Diagram of coordinate system of AMM part [52]

A material's elastic properties are typically evaluated using some kind of destructive tensile test. Using ultrasound, the longitudinal speed c_p and shear speed c_s of sound in a material can be measured and used to compute its Young's modulus E and Poisson's ratio υ as given by Equations 3.2 and 3.3 [53]. These expressions were derived empirically for an isotropic material which has only one distinct pressure and shear wave speed, so their

applicability for 316L produced by SLM is limited.

$$E = \frac{\rho c_s^2 (3c_p^2 - 4c_s^2)}{c_p^2 - c_s^2} \tag{3.2}$$

$$\upsilon = \frac{(3c^2 - 4c^2)}{2(c_p^2 - c_s^2)} - 1 \tag{3.3}$$

By substituting the measured speeds of sound from Table 3.1, into Equations 3.2 and 3.3, estimates of the material's elastic properties E_1, E_2, υ_1 and υ_2 were produced and are listed in Table 3.2. Using the measured value of $c_{p_{x,y}}$ results in E_1 and υ_1, which differ from the values of E_2 and υ_2 computed using $c_p = c_{p_z}$. This discrepancy reinforces the notion that there is mechanical and acoustic anisotropy in AMM parts. $E_{x,y}$ and E_z are published values for 316L produced by SLM while υ is an average value for the alloy.

Table 3.2: Elastic properties of additively manufactured SS 316L estimated from speeds of sound.

Young's Modulus				Poisson's Ratio		
$E_{x,y}$ [ksi]	E_z [ksi]	E_1 [ksi]	E_2 [ksi]	υ	υ_1	υ_2
26800	26100	27000 ± 5000	28000 ± 4000	0.25	0.25 ± 0.04	0.31 ± 0.01

3.3 Comparison to Theoretical Predictions

For an isotropic solid, the speed of a pressure or longitudinal wave c_p is given by Equation 3.4 in terms of the material's density ρ, modulus of elasticity E, and Poisson's ratio υ. The speed of a shear or transverse wave c_s in the solid is given by Equation 3.5 in terms of the same material properties [54].

$$c_p = \sqrt{\frac{E(1-\upsilon)}{\rho(1+\upsilon)(1-2\upsilon)}} \tag{3.4}$$

$$c_s = \sqrt{\frac{E}{2\rho(1+\upsilon)}} \tag{3.5}$$

At any point, a material's strain tensor [ ] is related to its stress tensor [σ] by its respective compliance tensor [S], as given by Equation 3.6. Additively manufactured metal structures are not purely isotropic but transversely isotropic wherein the elastic properties are symmetric about the axis normal to the build direction. Expanding Equation 3.6 for a transversely isotropic material yields Equation 3.7. The components of the compliance tensor only depend on the modulus of elasticity in the plane of the layers E_1, the modulus of elasticity perpendicular to the layers E_3, Poisson's ratio in the plane of the layers υ_1, and Poisson's ratio with elongation along the layers and contraction along the build axis υ_{13}. These properties are simple to measure and are convenient for engineering analysis.

$$[\ ] = [S][\sigma] \tag{3.6}$$

$$\begin{bmatrix} \varepsilon_{11} \\ \varepsilon_{22} \\ \varepsilon_{33} \\ 2\varepsilon_{23} \end{bmatrix} = \begin{bmatrix} \frac{1}{E_1} & \frac{-\nu_1}{E_1} & \frac{-\nu_{13}}{E_1} & 0 & 0 & 0 \\ \frac{-\nu_1}{E_1} & \frac{1}{E_1} & \frac{-\nu_{13}}{E_1} & 0 & 0 & 0 \\ \frac{-\nu_{13}}{E_1} & \frac{-\nu_{13}}{E_1} & \frac{1}{E_3} & 0 & 0 & 0 \\ 0 & 0 & 0 & \frac{E_1}{2(1+\nu_{13})} & 0 & 0 \end{bmatrix} \begin{bmatrix} \sigma_{11} \\ \sigma_{22} \\ \sigma_{33} \\ \sigma_{23} \end{bmatrix} \tag{3.7}$$

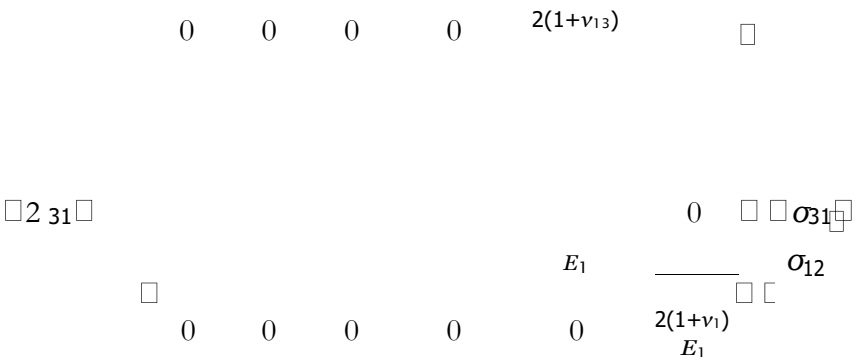

The principal speeds of sound in a transversely isotropic solid are found to satisfy

Christoffel's equations and are expressed in terms of the components of the stiffness tensor

$[C]$ [55]. The stiffness tensor is cumbersome to calculate on its own, so it can be computed

simply by inverting the compliance tensor as given by Equation 3.8.

$$[C] = [S]^{-1} \tag{3.8}$$

In the context of an AMM part, the first principal speed of sound c_1 is of a pure pressure wave which propagates along the layers. The second and third sound speeds c_2 and c_3 are pure shear modes which propagate in the build direction and along the layers, respectively. They are given by Equations 3.9–3.11 in terms of the stiffness matrix components C_{ij}.

$$c_1 = \sqrt{\frac{C_{11} + C_{12} + 2C_{44}}{2\rho}} \tag{3.9}$$

$$c_2 = \sqrt{\frac{C_{44}}{\rho}} \tag{3.10}$$

$$c_3 = \sqrt{\frac{C_{11} - C_{12}}{2\rho}} \tag{3.11}$$

A comparison of measured and calculated speeds of sound requires knowledge of the material's elastic properties. Unfortunately, only the Young's moduli in each respective direction are readily available, while Poisson's ratios are not. For standard isotropic 316L, the nominal Poisson's ratio is 0.25. While it is likely that υ_1 and υ_{13} are different, they are both assumed to be 0.25 for the sake of a simple approximation. Table 3.3 lists the measured, calculated, and researched speeds of sound for the additively manufactured 316L material. With the amount of precision available, there is no statistically significant difference between the theoretical and experimental speeds of sound for this material. Since theory does not provide a convenient expression for the pressure wave speed through the layers and experiments did not enable the measurement of shear wave speed through the layers, a complete assessment of the material's anisotropy couldn't be performed.

The published speeds of sound were calculated from values for Young's modulus, Poisson's

Table 3.3: Comparison of measured, calculated, and published speeds of sound for additively manufactured stainless steel type 316L.

	$c_{p_{x,y}}$ [in/μs]	c_{p_z} [in/μs]	$c_{sx,y}$ [in/μs]	c_{sz} [in/μs]
Measured	0.21 ± 0.01	0.227 ± 0.001	0.120 ± 0.001	–
Calculated ($\nu_1 = \nu_{13} = 0.25$)	0.21	–	0.12	0.12
Published	0.21	0.21	0.12	0.12

ratio, and density produced by from AK Steel and accessed via MatWeb [56]. The precision of these values limits the precision of the reference speeds of sound to two decimal places. It should also be noted that this particular alloy has a slightly greater modulus and density as compared to the additively manufactured material. Some of this discrepancy can be attributed to fact that these are bulk values and AMM structures are known to contain more void space. Despite this, the measured pressure wave speed along the layers shows good agreement with the isotropic value while the measured speed through the layers is considerably higher. An unfortunate limitation of the mini IIW-2 reference block is that its geometry only allows for measurement of shear wave speed along the layers. Since these speeds are identical for isotropic metal materials, this consideration was not made by the designers. A calibration standard optimized for AMM parts should include a curved feature such that it can reflect shear waves traveling through the layers. It is anticipated that the speed of a shear wave propagating through the layers would be greater than the speed in the plane of the layers and would vary with angle of incidence to each successive layer due to diffraction and scattering.

3.4 Scans of Notable Features

Four geometric features of the mini IIW-2 block were selected for direct comparisons of ultrasound inspections between the two materials. Figure 3.5 shows the areas that were inspected: 2" radius arc, 1/16" diameter hole, 1/8" diameter hole, and 1" diameter hole. A

5MHz phased array probe with a 36° angled wedge was used to inspect these features. A sector scan image was produced at each location with the probe positioned such that the amplitude of the reflection was roughly at its peak. A gate was set on the Mentor interface surrounding the reflection signal so that when the other block was inspected, the sound path was identical. With the same probe position, sound path length, and pulser-receiver settings, direct comparisons were made between the two blocks. It is clear that the additively manufactured 316L is more attenuative than the 1018 steel, as each reflection had a distinctly lower amplitude on the order of at least 0.4Np.

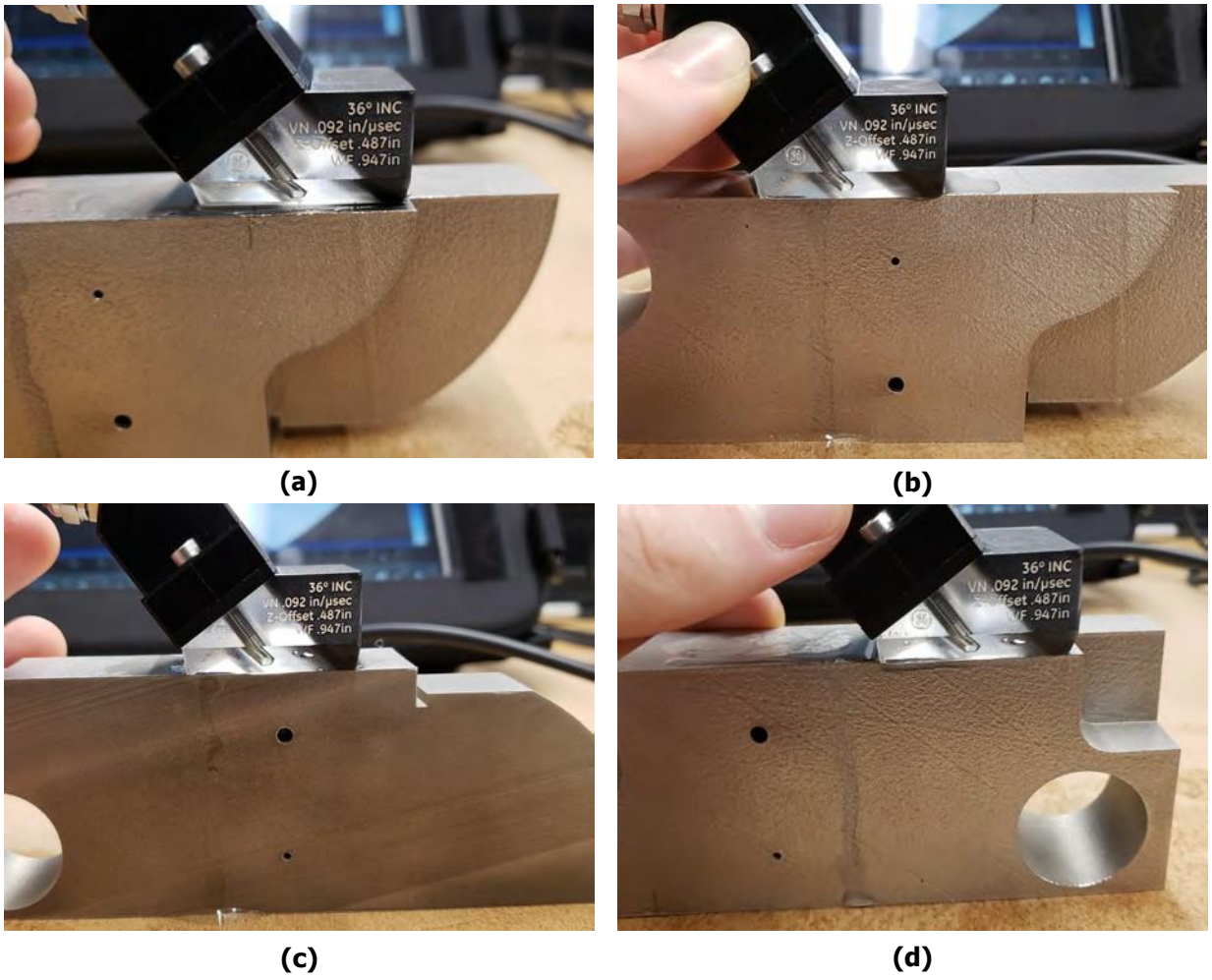

Figure 3.5: Notable features of the mini IIW-2 block. 2" radius arc (3.5a), 1/16" hole (3.5b), 1/8" hole (3.5c), and 1" hole (3.5d).

Table 3.4 summarizes the results of the sector scan inspections for the two mini IIW-2 blocks. The sound path measurements have an uncertainty of ±0.01" and the amplitude measurements have an uncertainty of ±0.5% as they were read from plots on the GE Mentor UT interface. The particular values of amplitude are not relevant, as they are measured in volts, amplified, and normalized. However, by only changing the reference block and its speed of sound while keeping the sound path and all other settings the same, the logarithmic ratio between these amplitudes, given in Nepers, is meaningful. Dividing the amplitude ratio by the sound path gives an attenuation constant for the additively manufactured 316L with 1018 steel as the reference. Figures 3.6-3.9 show side-by-side comparisons of the sector scans taken at each respective location on the mini IIW-2 blocks.

Table 3.4: Comparison of pulse-echo amplitudes at notable features of mini IIW-2 blocks.

Feature		2" Radius	1" Hole	1/8" Hole	1/16" Hole
Sound Path [in]		2.00	1.33	0.59	0.65
Amplitude	AISI 1018	71.5%	19.5%	15.5%	13.0%
	SLM SS 316L	47.5%	13.5%	6.5%	8.5%
Amplitude Ratio [Np]		0.41 ± 0.01	0.37 ± 0.05	0.87 ± 0.08	0.42 ± 0.07
Attenuation [Np/in]		0.20 ± 0.01	0.28 ± 0.03	1.5 ± 0.1	0.7 ± 0.1

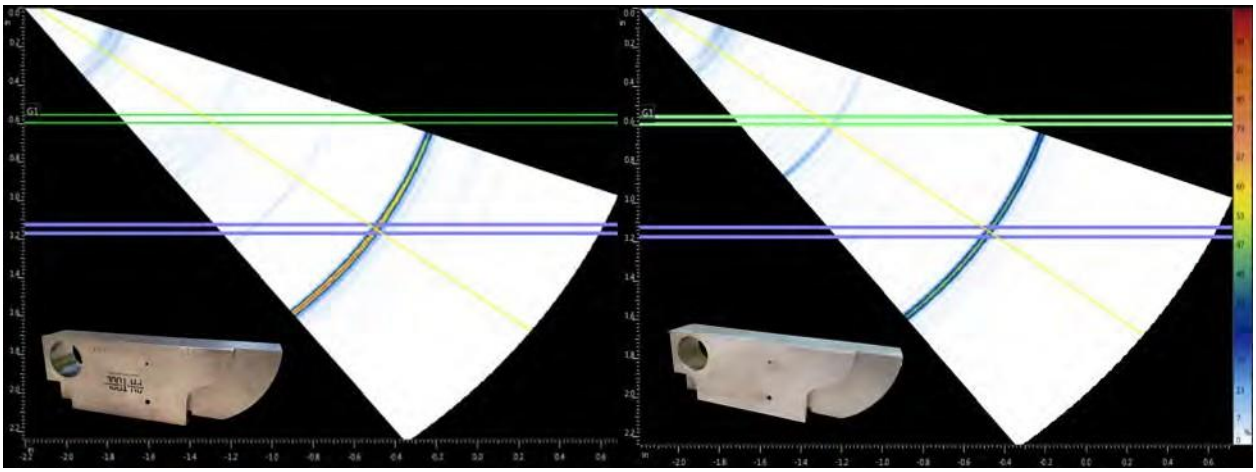

Figure 3.6: Sector scans of 2" radius. Original on left, AM on right.

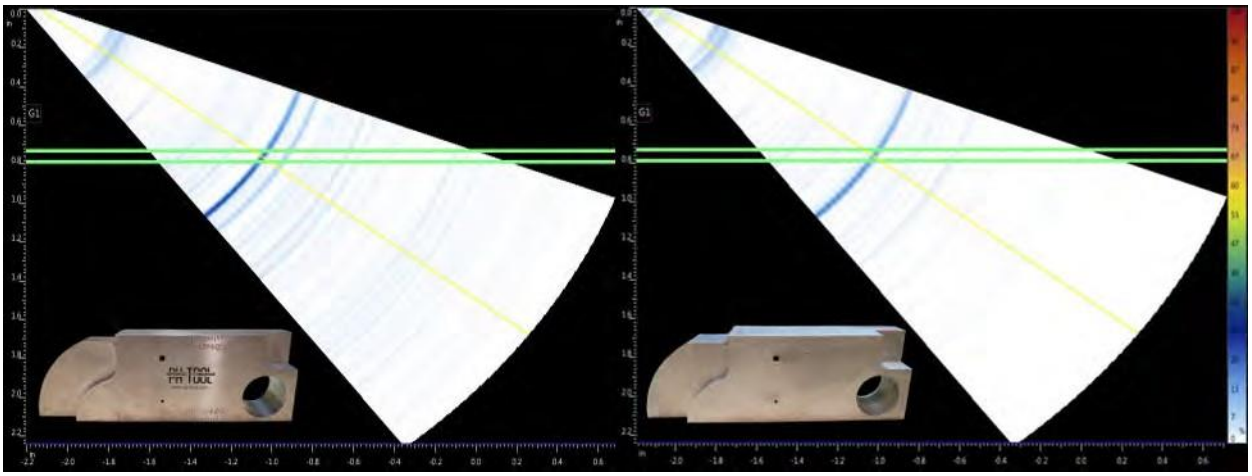

Figure 3.7: Sector scans of 1" hole. Original on left, AM on right.

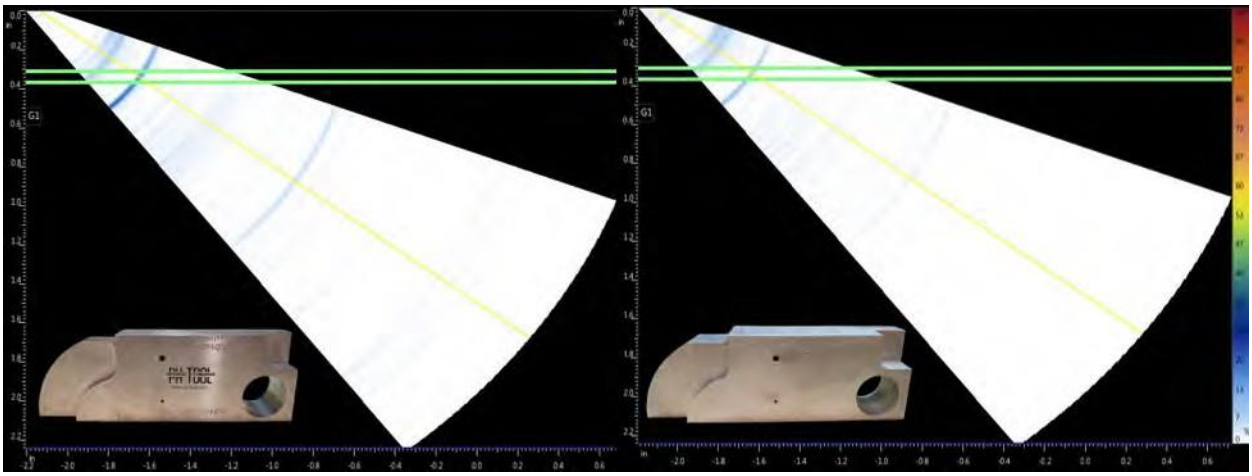

Figure 3.8: Sector scans of 1/8" hole. Original on left, AM on right.

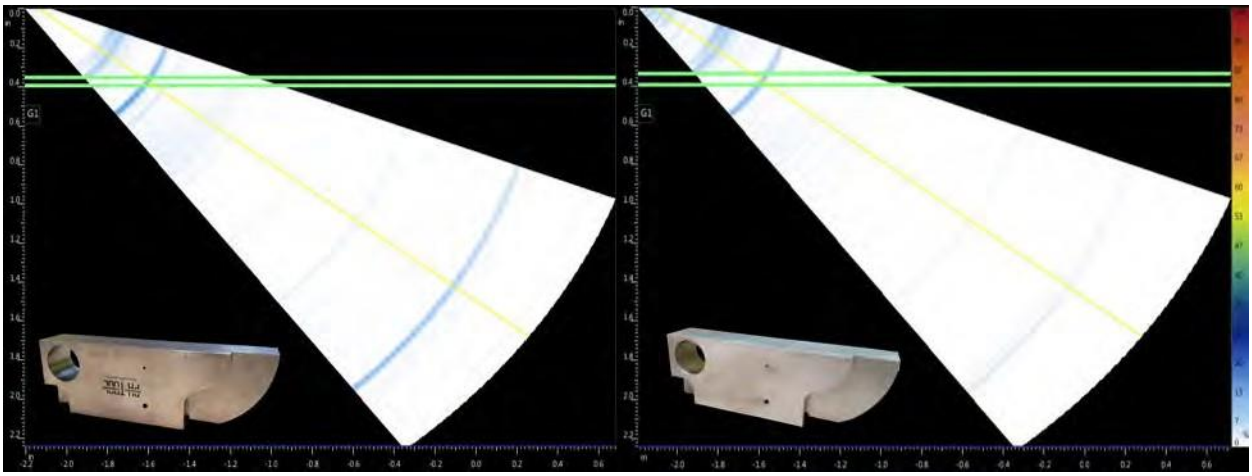

Figure 3.9: Sector scans of 1/16" hole. Original on left, AM on right.

Chapter 4

Wave Propagation Simulations

Numerical simulations of elastic wave propagation were explored as a way to corroborate experimental results. Various computational approaches have been applied to this area, most notably the finite element (FE) method and elastodynamic finite integration technique (EFIT). FE has been demonstrated for simulating acoustic wave propagation in dissimilar materials and through flawed domains as well in a highly scattering polycrystalline microstructure [57,58]. Benchmark comparisons of custom EFIT code to commercially available FE packages shows good agreement with one another and with experimental results regarding guided waves in polymer composites [59]. In the scope of this project, the time explicit elastic waves module in COMSOL Multiphysics was investigated for its applicability to modeling an angle beam UT inspection of a mini IIW-2 block.

4.1 Problem Geometry and Setup

To approximate a 45degree angle beam configuration, the geometry of an acrylic wedge and a mini IIW-2 block in the region of the $1/16$" and $1/8$" diameter cross-holes were modeled. To simplify the calculation, only the midplane of the wedge and block were designated as computational domains, with the steel block domain truncated to surround only the flaws of interest. The acrylic and steel domains were meshed such that the elements were no larger than the wavelength of a shear wave in the respective materials at the center frequency divided by 1.5. Figure 4.1 shows the domain geometry and the mesh for a probe frequency of 2.25MHz. To model far-field continuity, the left-hand and right-hand boundaries of the steel

domain were prescribed low-reflecting boundary conditions. This same boundary condition was applied to the outer walls of the acrylic wedge to model damping, with the exception of the angled transducer edge. This edge was assigned a time-dependent normal velocity

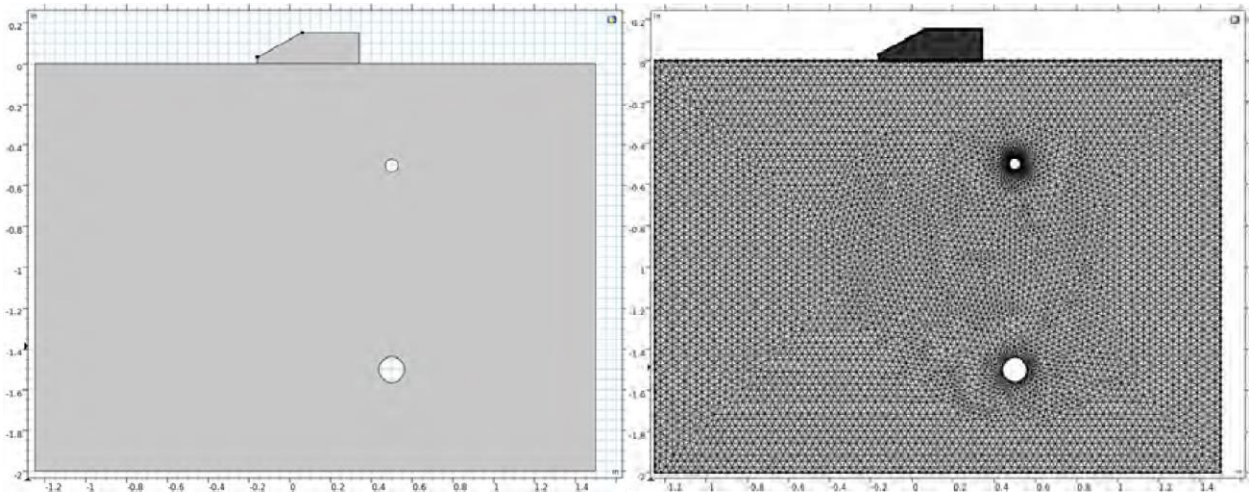

(a) (b)

Figure 4.1: Geometry (4.1a) and mesh (4.1b) for a 2.25MHz probe frequency.

boundary condition to represent the pulses from a piezoelectric element. The velocity v_0 takes the form of a Gaussian-modulated sine function centered around a given frequency f_0 with period T_0, as given by Equation 4.1.

$$v_0 = e^{-\left\{\frac{2(t-2T_0)}{T_0}\right\}^2} \sin(2\pi f_0 t) \tag{4.1}$$

For a probe frequency of 2.25MHz, a transient calculation of acoustic pressure was performed over a time period of $30T_0$ with a time step of $T_0/20$. Figure 4.2 shows plots of pressure at different points in time as the wave from the initial pulse propagates through the domains. Figure 4.3 shows a plot of average pressure over the transducer edge versus time, showing a reflection from the 1/16" diameter hole at roughly 10.5µs after the initial pulse. Running on a system with 16Gb of RAM, each solution takes several hours to compute. Higher frequency models require finer meshes which incur longer computation times.

Additionally, higher frequency pulses are attenuated more which drastically diminishes the flaw echo.

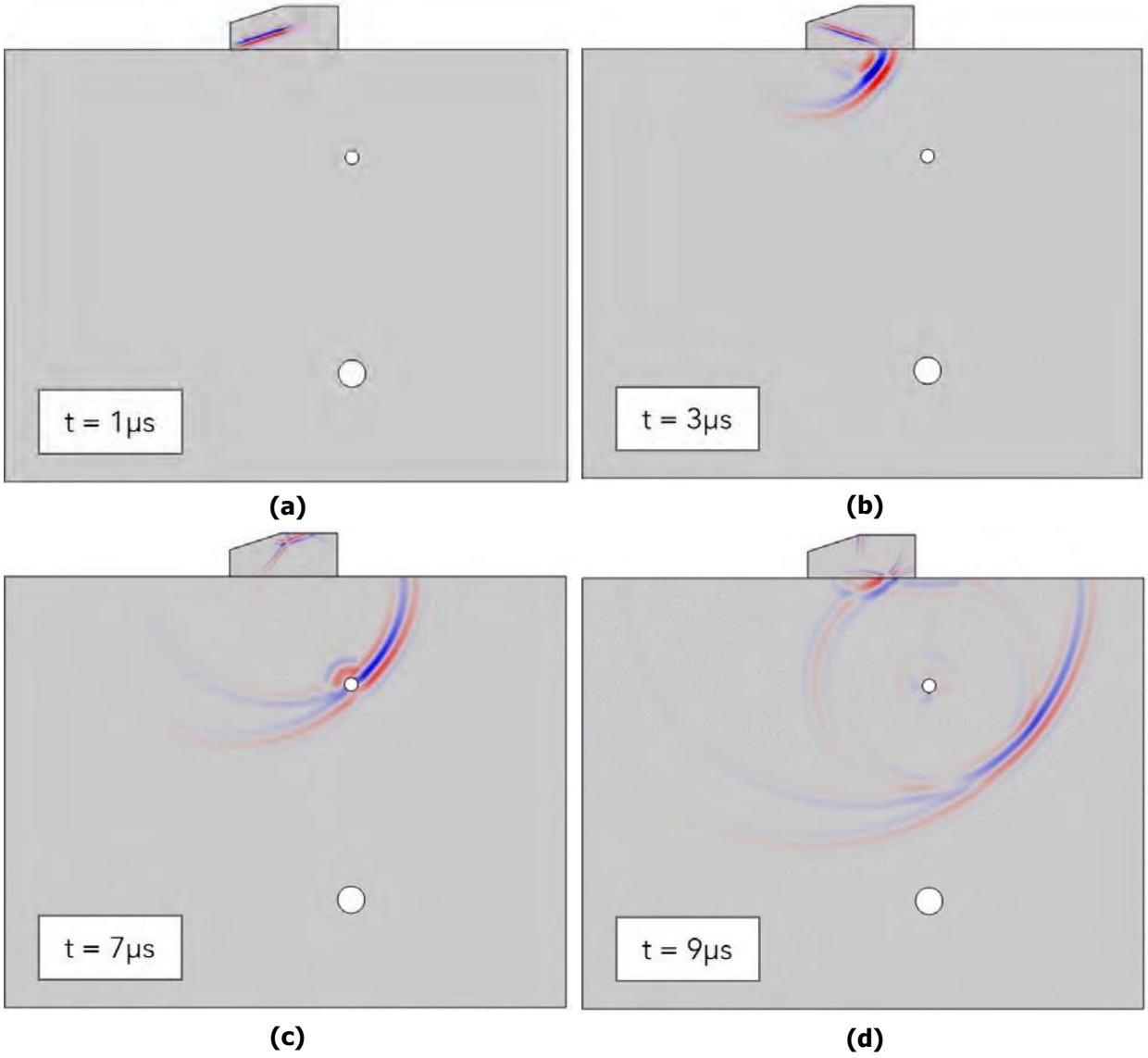

Figure 4.2: Plots of acoustic pressure across the midplane at $1\mu s$ (4.2a), $3\mu s$ (4.2b), $7\mu s$ (4.2c), and $9\mu s$ (4.2d) after the initial pulse. Color scale is blue to red from low pressure to high pressure on a range of $-2MPa$ to $+2MPa$.

As a proof of concept, the steel domain in this model was assigned isotropic material properties: namely, the Poisson's ratio and density of standard 316L stainless steel and the Young's modulus of additively manufactured 316L along the layers. To more accurately

model the behavior of the material, anisotropic material properties should be assigned to the domain and a fully 3D simulation should be run. Acoustic phenomena such as absorption and scattering are not captured in a 2D calculation and their effects are expected to be considerable in additively manufactured metal. Such a 3D model could be developed in COMSOL or using custom EFIT code developed by Raley and Dieckman in 2019 [60]. In the meantime, preliminary simulation results appear reasonable when compared to ultrasound inspections of the additively manufactured 316L mini IIW-2 block.

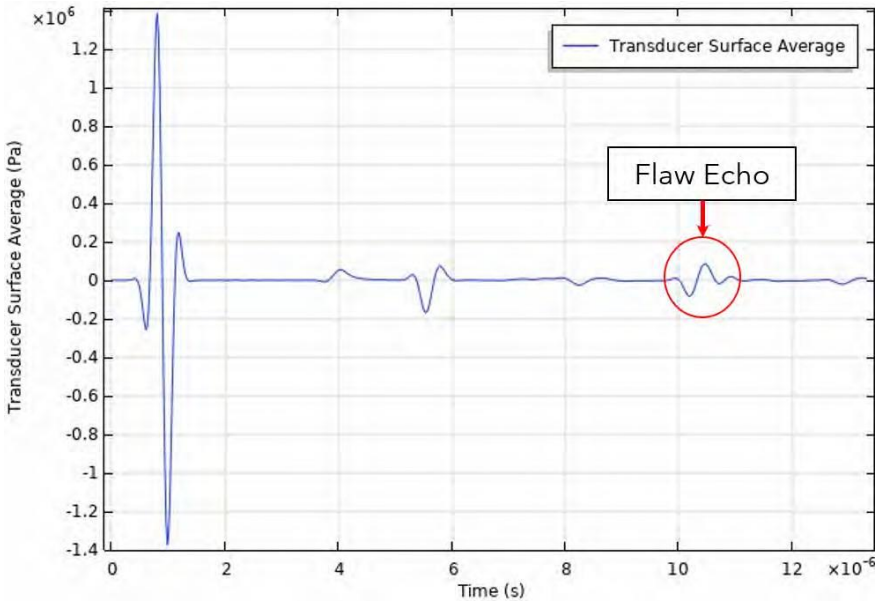

Figure 4.3: Average pressure on transducer surface over time for 2.25MHz pulse. A large spike is seen at the initial pulse with several small fluctuations as sound energy reflects from the top of the steel block and within the acrylic wedge. The spike at roughly 10.5μs indicates the reflection from the 1/16" diameter hole.

Chapter 5

Conclusions and Recommendations

5.1 Immersion Tank

A custom immersion testing system that is compatible with all the UT equipment already in use at University of New Haven was designed and built for approximately $1000. The lack of resolution is a limitation of the user interface and not any of the hardware. Therefore, the system is satisfactory for detecting the types and sizes of defects that are most critical for part failure. Further modification of the apparatus is made simple through the use of open-source hardware and electronics. A new ultrasound system that operates in tandem with the gantry motors would be ideal. This way, the pulser-receiver could be triggered through the motor control code and there would be no risk of losing synchronization between the ultrasound signals and the probe positioning. The rotary encoder compatible with the GE Mentor UT has a lower resolution than the linear actuators of the immersion tank and has the potential to slip or lose steps, so the incorporation of closed-loop stepper motors would ensure the system's precision. Another limitation of the Mentor is the inability to extract numerical data from it. The analysis done in this project was done using values read from the plots on the tablet interface. The ability to export full A-scan data would enable more detailed analysis and the creation of custom C-scan plots.

5.2 UT Reference Standards for AMM

Due to the unique microstructure of AMM parts, new reference standards for UT should be created for each alloy, fabrication method, and post-processing treatment. In the short term, existing designs for calibration blocks may be used with caution. Additively manufactured metal has been shown to be more attenuative to sound waves than conventionally produced metal and has clear anisotropy in its mechanical and acoustic properties. The different speeds of sound should be calibrated for and a relatively high gain should be used in UT inspections. A completely new calibration block for additively manufactured metal must include features that enable measurements of longitudinal and shear wave speed in at least three principal directions. For reference, a block might contain crack-like defects at different depths and orientations with respect to the layers, as crack tip diffraction has not been fully investigated and characterized in AMM parts.

5.3 Application of UT to AMM Parts

Ultrasonic methods are promising for detecting voids and crack-like flaws in additively manufactured metal parts. While ultrasound is not necessarily useful for characterizing porosity, micron-scale pores are not typically concerning from a fatigue failure standpoint. Standards for AMM part production are steadily being adopted, so the responsibility of minimizing porosity may soon be taken on completely by suppliers, with XCT being used periodically to ensure the product exceeds an established density threshold. While UT is not a convenient method for imaging intricate objects, it appears to be applicable for inspecting fracture-critical components for cracks and lack-of-fusion voids in key load-bearing areas. Contact ultrasound methods or immersion testing may be used in these cases depending on the orientation of a critical flaw. The automated nature of immersion testing enables fairly quick repeated inspections and therefore is appealing for types of components which

must go through NDE before being put into service. The definition of a critical flaw size, location, and orientation must be determined by the mechanical designers of a component. This definition requires consulting fatigue and fracture data for each material and process used in AM, which is currently collected internally by organizations using AM but may soon be made more universally available. For such a critical flaw, elastic wave simulations could be conducted to provide a theoretical prediction for the associated ultrasound signal. In conjunction with AM-specific reference standards, additively manufactured parts can be certified with confidence using UT for applications with a high risk of failure.

Appendix

A: Immersion Tank Motor Control Code

```
// ----- * Stepper Motor Control for Immersion Tank * ----
// By: Malak Souissi - 02/24/2019
// Modified by Austin Thomas - 11/09/2020
// Allows the control of both the X and Y actuators using the box
   controller
// and the MATLAB GUI   (UT_NDE_GUI.fig)

#include <Metro.h>

// ------------ Homing and Limit Switch Declarations --------
float CurrentPosX;
int LowerLimitX = 26;       // Lower limit switch for X axis
int UpperLimitX = 28;       // Upper limit switch for X axis
int CalibrationLED1 = 44;

float CurrentPosY;
int LowerLimitY = 22;       // Lower limit switch for Y axis
int UpperLimitY = 24;       // Upper limit switch for Y axis
int CalibrationLED2 = 45;

bool SetHomeX = LOW;
bool SetHomeY = LOW;

// -------- Mode Declarations -----------------
bool RunMode;
```

```
bool SetMode;

// ------- Stepper Motor Driver Assignments ---------------
long ppmm = 250;            // Motor pulses per mm of linear  travel
                            // (microsteps/rev)*(1rev /8mm)
const int stepX = 14;       // Pin for step signal for X motor  driver
const int direction X= 15;  // Pin for direction signal for X motor driver
const int enableX = 16;     // Pin for enable signal for X motor driver

const int stepY = 51;       // Pin for step signal for Y motor  drivers
const int direction Y= 53;  // Pin for direction signal for Y motor
   drivers
const int enableY = 52;     // Pin for enable signal for Y motor drivers

// ------------ Button and Switch Assignments ----------------------
const int MotorSwitch_X = 13; // Motor switch: X (M1) (Yellow Wire)
const int MotorSwitch_Y = 12; // Motor switch: Y (M2) (Black Wire)
const int RotatePlus = 11;    // +Rotate button (White Wire)
const int RotateMinus = 10;   // -Rotate button (Green Wire)
const int Set Home =9;        // Set Home button (Black Wire)
const int Go Home =8;         // Go Home button (Blue Wire)
const int RunSwitch_R = 7;    // Run switch: Run mode (Yellow Wire)
const int RunSwitch_S = 6;    // Run switch: Set mode (Red Wire)

// ----------- Potentiometer   Assignments ------------------------
int SpeedPin = A0;            // Jog Speed knob (Yellow Wire)
int AnglePin = A1;            // Jog Angle knob (Blue Wire)
int SpeedValue  = 0;
int AngleValue = 0;


// -------- Motor Move Function  --------
```

```
void MotorMove(int Actuator, bool Direction, int Speed, long NumberofSteps
    )
// Specify the actuator (1=X, 2=Y), direction (HIGH or LOW), speed (delay
    in microseconds ),
// and number of steps to move ( int )
{
  float RampSlope;
  int RampSpeed;
  if (Actuator == 1)  // X axis  actuator
  {
    bool UpperLimitReachedX = digitalRead(UpperLimitX);
    bool LowerLimitReachedX = digitalRead(LowerLimitX);      // LOW means
    a limit has been  reached
    digitalWrite(directionX, Direction);                     // Set  the
    direction pin of the stepper  driver
    for (int x = 0; x <= round(NumberofSteps/16); x++)       // First 1/16
    th of the move is a ramp up
    {
      RampSlope = (float(Speed)-1000.0)/(float(NumberofSteps)/16.0);  //
    Slope of the ramp from 1000 microsecond delay to nominal speed
      RampSpeed = round(RampSlope*x + 1000);                         //
    Linearly decreasing delay rounded to nearest microsecond
      digitalWrite(stepX, HIGH);
      delayMicroseconds(RampSpeed);
      digitalWrite(stepX, LOW);
      delayMicroseconds(RampSpeed);
      LowerLimitReachedX = digitalRead(LowerLimitX);   // Check each
    iteration if lower limit has been  reached
      if (LowerLimitReachedX == LOW)
        {
```

```
79          digitalWrite(directionX, LOW);                  // Jog +5mm at
    nominal speed if lower limit is reached
            for (int x = 0; x < (5*ppmm); x++)
81          {
            digitalWrite(stepX, HIGH);
83          delayMicroseconds(Speed);
            digitalWrite(stepX, LOW);
85          delayMicroseconds(Speed);
            }
87          break;           // Stop the move entirely
            }
89        UpperLimitReachedX=digitalRead(UpperLimitX);   // Check each
    iteration if upper limit has been reached
          if (UpperLimitReachedX == LOW)
91          {
            digitalWrite(directionX, HIGH);     // Jog -5mm at nominal speed
    if upper limit is reachhed
93          for (int x = 0; x < (5*ppmm); x++)
            {
95          digitalWrite(stepX, HIGH);
            delayMicroseconds(Speed);
97          digitalWrite(stepX, LOW);
            delayMicroseconds(Speed);
99          }
            break;          // Stop the move entirely
101         }
         }
103      for (int x = 0; x <= round(0.875*NumberofSteps); x++)  // Next 7/8ths
    of the move is at nominal speed
         {
105        digitalWrite(stepX, HIGH);
           delayMicroseconds(Speed);
```

```
107       digitalWrite(stepX, LOW);
          delayMicroseconds(Speed);
109       LowerLimitReachedX = digitalRead(LowerLimitX);  // Check each
iteration if lower limit has been  reached
          if (LowerLimitReachedX == LOW)
111         {
            digitalWrite(directionX, LOW);              // Jog +5mm at nominal
speed if lower limit is reached
113         for (int x = 0; x < (5*ppmm); x++)
            {
115         digitalWrite(stepX, HIGH);
            delayMicroseconds(Speed);
117         digitalWrite(stepX, LOW);
            delayMicroseconds(Speed);
119         }
            break;          // Stop the move  entirely
121         }
          UpperLimitReachedX = digitalRead(UpperLimitX);   // Check  each
iteration if upper limit has been  reached
123       if (UpperLimitReachedX == LOW)
            {
125         digitalWrite(directionX, HIGH);             // Jog -5 mmat
nominal  speed if upper limit is  reachhed
            for (int x = 0; x < (5*ppmm); x++)
127         {
            digitalWrite(stepX, HIGH);
129         delayMicroseconds(Speed);
            digitalWrite(stepX, LOW);
131         delayMicroseconds(Speed);
            }
133         break;
            }
```

```
135     }
        for (int x = 0; x < round(NumberofSteps/16); x++)    // Last 1/16th of
        the move is a ramp down
137     {
          RampSlope = (1000.0-float(Speed))/(float(NumberofSteps)/16.0); //
        Slope of the ramp from nominal speed to 1000 microsecond delay
139       RampSpeed = round(RampSlope*x + Speed);                          //
        Linearly increasing delay rounded to nearest microsecond
          digitalWrite(stepX, HIGH);
141       delayMicroseconds(RampSpeed);
          digitalWrite(stepX, LOW);
143       delayMicroseconds(RampSpeed);
          LowerLimitReachedX=digitalRead(LowerLimitX);   // Check each
        iteration if lower limit has been  reached
145       if (LowerLimitReachedX == LOW)
            {
147         digitalWrite(directionX, LOW);            // Jog +5mm at nominal
        speed if lower limit is reachhed
            for( int x = 0; x < (5*ppmm); x++)
149         {
            digitalWrite(stepX, HIGH);
151         delayMicroseconds(Speed);
            digitalWrite(stepX, LOW);
153         delayMicroseconds(Speed);
            }
155         break;                  // Stop the move entirely
            }
157       UpperLimitReachedX=digitalRead(UpperLimitX);  // Check each
        iteration if upper limit has been reached
          if (UpperLimitReachedX == LOW)
159         {
```

```
        digitalWrite(directionX, HIGH);        // Jog -5 mm at nominal
    speed if upper limit is reachhed
161     for (int x = 0; x < (5*ppmm); x++)
        {
163     digitalWrite(stepX, HIGH);
        delayMicroseconds(Speed);
165     digitalWrite(stepX, LOW);
        delayMicroseconds(Speed);
167     }
        break;
169     }
     }
171  }
   else if (Actuator == 2)  // Y axis  actuator
173  {
     bool UpperLimitReachedY = digitalRead(UpperLimitY);
175  bool LowerLimitReachedY = digitalRead(LowerLimitY);      // LOW means
    a limit has been  reached
     digitalWrite(directionY, Direction);                    // Set the
    direction pin of the stepper  driver
177  for (int x = 0; x <= round(NumberofSteps/16); x++)       // First 1/16
    th of the move is a ramp up
     {
179    RampSlope = (float(Speed)-1000.0)/(float(NumberofSteps)/16.0);  //
    Slope of the ramp from 1000 microsecond delay to nominal speed
       RampSpeed = round(RampSlope*x + 1000);                          //
    Linearly decreasing delay rounded to nearest microsecond
181    digitalWrite(stepY, HIGH);
       delayMicroseconds(RampSpeed);
183    digitalWrite(stepY, LOW);
       delayMicroseconds(RampSpeed);
```

```
185       LowerLimitReachedY=digitalRead(LowerLimitY);   // Check each
    iteration if lower limit has been  reached
          if (LowerLimitReachedY == LOW)
187         {
            digitalWrite(directionY,LOW);      // Jog +5mm at nominal speed
    if lower limit is  reached
189         for (int x = 0; x < (5*ppmm); x++)
            {
191         digitalWrite(stepY, HIGH);
            delayMicroseconds(Speed);
193         digitalWrite(stepY, LOW);
            delayMicroseconds(Speed);
195         }
            break;              // Stop the move  entirely
197         }
          UpperLimitReachedY=digitalRead(UpperLimitY);   // Check each
    iteration if upper limit has been reached
199       if (UpperLimitReachedY == LOW)
            {
201         digitalWrite(directionY,HIGH);     // Jog -5mm at nominal speed
    if upper limit is  reachhed
            for (int x = 0; x < (5*ppmm); x++)
203         {
            digitalWrite(stepY, HIGH);
205         delayMicroseconds(Speed);
            digitalWrite(stepY, LOW);
207         delayMicroseconds(Speed);
            }
209         break;            // Stop the move  entirely
            }
211    }
```

```
    for (int x = 0; x <= round(0.875*NumberofSteps); x++)    // Next 7/8ths
    of the move is at nominal  speed
213 {
      digitalWrite(stepY, HIGH);
215   delayMicroseconds(Speed);
      digitalWrite(stepY, LOW);
217   delayMicroseconds(Speed);
      LowerLimitReachedY=digitalRead(LowerLimitY);  // Check each
    iteration if lower limit has been  reached
219   if (LowerLimitReachedY == LOW)
        {
221     digitalWrite(directionY, LOW);              // Jog +5mm at nominal
     speed if lower limit is reached
        for (int x = 0; x < (5*ppmm); x++)
223     {
        digitalWrite(stepY, HIGH);
225     delayMicroseconds(Speed);
        digitalWrite(stepY, LOW);
227     delayMicroseconds(Speed);
        }
229     break;          // Stop the move entirely
        }
231   UpperLimitReachedY = digitalRead(UpperLimitY);    // Check  each
    iteration if upper limit has been  reached
      if (UpperLimitReachedY == LOW)
233     {
        digitalWrite(directionY, HIGH);             // Jog -5 mm at
    nominal  speed if upper limit is  reachhed
235     for (int x = 0; x < (5*ppmm); x++)
        {
237     digitalWrite(stepY, HIGH);
        delayMicroseconds(Speed);
```

```
239         digitalWrite(stepY, LOW);
            delayMicroseconds(Speed);
241         }
            break;
243         }
        }
245     for (int x = 0; x < round(NumberofSteps/16); x++)     // Last 1/16th of
        the move is a ramp down
        {
247        RampSlope = (1000.0-float(Speed))/(float(NumberofSteps)/16.0); //
    Slope of the ramp from nominal speed to 1000 microsecond delay
           RampSpeed = round(RampSlope*x + Speed);              // Linearly
    increasing delay rounded to nearest microsecond
249        digital  Write  (  stepY  ,  HIGH  );
           delay Microseconds ( Ramp  Speed  );
251        digital  Write  (  stepY  ,  LOW  );
           delayMicroseconds(RampSpeed);
253        LowerLimitReachedY = digitalRead(LowerLimitY);   // Check each
    iteration if lower limit has been  reached
           if (LowerLimitReachedY == LOW)
255          {
             digitalWrite(directionY, LOW);          // Jog +5mm at nominal
    speed if lower limit is reachhed
257          for( int x = 0; x < (5*ppmm); x++)
             {
259          digitalWrite(stepY, HIGH);
             delayMicroseconds(Speed);
261          digitalWrite(stepY, LOW);
             delayMicroseconds(Speed);
263          }
             break;              // Stop the move  entirely
265          }
```

```
      UpperLimitReachedY=digitalRead(UpperLimitY);  // Check each
    iteration if upper limit has been  reached
267     if (UpperLimitReachedY == LOW)
        {
269     digitalWrite(directionY,HIGH);      // Jog -5mm at nominal speed
    if upper limit is  reachhed
        for (int x = 0; x < (5*ppmm); x++)
271     {
        digitalWrite(stepY, HIGH);
273     delayMicroseconds(Speed);
        digitalWrite(stepY, LOW);
275     delayMicroseconds(Speed);
        }
277     break;
        }
279   }
    }
281 }

283 // ----------- Getting Strings Over Serial --------------
  String getValue(String data, char separator, int index) {
285   int found =  0;
    int strIndex[] = {0,-1};
287   int maxIndex= data.length() - 1;

289   for (int i=0; i<= maxIndex && found <= index; i++) {
      if (data.charAt(i) == separator || i == maxIndex) {
291   found                ++;
      strIndex[0]=strIndex[1] + 1;
293   strIndex[1]= (i == maxIndex) ? i+1 : i;
      }
295   }
```

```
    return found > index ? data.substring(strIndex[0], strIndex[1]) : "";
297 }

299 Metro MATLABSerial = Metro(500);

301 void setup () {

303   CurrentPosX = 0;
      CurrentPosY = 0;
305
      // Limit Switch Setup
307   pinMode(LowerLimitX, INPUT);
      pinMode(UpperLimitX, INPUT);
309   pinMode(LowerLimitY, INPUT);
      pinMode(UpperLimitY, INPUT);
311
      // Calibration LEDs Setup
313   pinMode(CalibrationLED1, OUTPUT);
      pinMode(CalibrationLED2, OUTPUT);
315   digitalWrite(CalibrationLED1, LOW);
      digitalWrite(CalibrationLED2, LOW);
317
      // Stepper Motor Drivers Setup
319   pinMode(stepX, OUTPUT);
      pinMode(directionX, OUTPUT);
321   pinMode(enableX, OUTPUT);
      digitalWrite(enableX, LOW);
323   pinMode(stepY, OUTPUT);
      pinMode(directionY, OUTPUT);
325   pinMode(enableY, OUTPUT);
      digitalWrite(enableY, LOW);
327
```

```
  // Button and Switch  Setup
  pinMode(MotorSwitch_X, INPUT_PULLUP);
  pinMode(MotorSwitch_Y, INPUT_PULLUP);
  pinMode(RotatePlus, INPUT_PULLUP);
  pinMode(RotateMinus, INPUT_PULLUP);
  pinMode(SetHome, INPUT_PULLUP);
  pinMode(GoHome, INPUT_PULLUP);

  pinMode(RunSwitch_R, INPUT_PULLUP);
  pinMode(RunSwitch_S, INPUT_PULLUP);

  Serial.begin(9600);
}

void loop () {

if(MATLABSerial.check()){}

  int isMotorSwitch_X = digitalRead(MotorSwitch_X);
  int isMotorSwitch_Y = digitalRead(MotorSwitch_Y);
  int isRotatePlus = digitalRead(RotatePlus);
  int isRotateMinus = digitalRead(RotateMinus);
  int isSetHome = digitalRead(SetHome);
  int isGoHome = digitalRead(GoHome);
  int isRunSwitch_R = digitalRead(RunSwitch_R);
  int isRunSwitch_S = digitalRead(RunSwitch_S);

     if (Serial.available())
     {

    String SerialIntake = Serial.readString();

```

```
    String val1 = getValue(SerialIntake, ':', 0);
    String val2 = getValue(SerialIntake, ':', 1);
    String val3 = getValue(SerialIntake, ':', 2);
    String val4 = getValue(SerialIntake, ':', 3);
    String val5 = getValue(SerialIntake, ':', 4);

  if ( val1 == " A") // If X axis is selected in GUI
   {
  // val2 indicates direction, val3 is the distance in mm, val4 is the speed (0 -100)
    int JogSpeed = round(-9.5*val4.toInt()+1000);    // Map 0 -100 speed to 1000 -50 microseconds delay
    long JogSteps = round(val3.toFloat()*ppmm);      // Multiply distance by pulses /mm and round to whole number

    if (val2 == "A")  // If + direction is selected in GUI
    {
     MotorMove(1, LOW, JogSpeed, JogSteps);
    }
   else if ( val2 == "B")  // If - direction is selected in  GUI
    {
     MotorMove(1, HIGH, JogSpeed, JogSteps);
    }
    else if (val2 == "C"){}  // If set home for X is selected in GUI, the position is set to 0 in the GUI . Nothing happens here.

    else if (val2 == "D") //If go home is selected for X in GUI
    // val3 indicates the current X position in mm
    {
     long HomeSteps = round(val3.toFloat()*ppmm);     // Number of steps required to go to home position
```

```
    if (val3.toFloat() > 0)                              // If X
displacement is positive
387      {
          MotorMove(1, HIGH, JogSpeed, HomeSteps);       // Run X motor in -
 direction
389      }
    else MotorMove(1, LOW, JogSpeed, abs(HomeSteps));  // If X
displacement is negative , run X motor in + direction
391    }
  }
393
  if (val1 == "B")  // If Y axis is selected in GUI
395  {
  int JogSpeed = round(-9.5*val4.toInt()+1000);
397  long JogSteps = round(val3.toFloat()*ppmm);     // Multiply distance
by pulses / mm and round to whole number

399    if (val2 == "A")  // If + direction is selected in GUI
    {
401     MotorMove(2, LOW, JogSpeed, JogSteps);
    }
403    else if ( val2 == "B")  // If - direction is selected in  GUI
    {
405     MotorMove(2, HIGH, JogSpeed, JogSteps);
    }
407    else if (val2 == "C"){}  // If set home for Y is selected in GUI ,
the position is set to 0 in the GUI . Nothing happens here .

409    else if (val2 == "D") //If go home is selected for Y in GUI
    // val3 indicates the current Y position in mm
411    {
```

```
    long HomeSteps = round(val3.toFloat()*ppmm);      // Number of steps
 required to go to home position
413     if (val3.toFloat() > 0)                                // If X
displacement is positive
      {
415    MotorMove(1, HIGH, JogSpeed, HomeSteps);        // Run X motor in
- direction
      }
417     else MotorMove(1, LOW, JogSpeed, abs(HomeSteps));   // If X
displacement is negative , run X motor in + direction
     }
419   }

421   // ----------- Scan Sequence -------------------
   if (val1 == "S") // If Start Scan, Scan Right, Scan Left, or Index Up
 button is pushed in  GUI
423   {
    if (val2 == "R"){ // Scan to the right (+x direction) by the scan
size
425     MotorMove(1, LOW, 1000, round(val3.toFloat()*ppmm));
      }
427    else if (val2 == "L"){ // Scan to the left (-x direction) by the
scan size
      MotorMove(1, HIGH, 1000, round(val3.toFloat()*ppmm));
429     }
    else if (val2 == "I"){ // Index up (+y direction) by the index
distance
431     MotorMove(2, LOW, 1000, round(val3.toFloat()*ppmm));
      }
433    else if (val2 == "A"){ // Auto Scan
      int y =  0;
435     delay(val4.toInt());
```

```
        while (y < round(val4.toFloat()/val5.toFloat()))
437       {
            if (( y % 2) == 0){ // Even numbered rows , X moves in +
  direction
439         MotorMove(1, LOW, 1000, val3.toFloat()*ppmm);
            }
441         else {    // Odd rows, X moves in - direction
            MotorMove(1, HIGH, 1000, val3.toInt()*ppmm);
443         }
            MotorMove(2, LOW, 1000, round(val5.toFloat()*ppmm));
445         y = y +1;
          }
447      }
       }
449   }

451   // ------------- Control Box -----------------

453 SpeedValue = analogRead(SpeedPin);
  SpeedValue = map(SpeedValue, 0, 1023, 100, 1000);
455 AngleValue = analogRead(AnglePin);
  AngleValue = map(AngleValue, 0, 1023, 10, 1);
457
    // -------- Run/Set Switch ----------
459 if (isRunSwitch_S == LOW) { // Run Mode
    RunMode = HIGH;
461   SetMode = LOW;
  } else {   // Set Mode
463   RunMode = LOW;
    SetMode = HIGH;
465 }
```

```
467   if (isMotorSwitch_X == LOW) { // If X Axis is Selected
        if (isRotatePlus == LOW) { // If + Rotate is Pressed
469       MotorMove(1, LOW, SpeedValue, AngleValue*ppmm);
          CurrentPosX = CurrentPosX + AngleValue;
471     }
        else if (isRotateMinus == LOW) { // If - Rotate is Pressed
473       MotorMove(1, HIGH, SpeedValue, AngleValue*ppmm);
          CurrentPosX = CurrentPosX - AngleValue;
475     }

477     else if (isSetHome == LOW && SetMode == HIGH ) { // If Set  Home Button
        is Pressed
          digitalWrite(CalibrationLED1, HIGH);
479       CurrentPosX = 0;
          SetHomeX = HIGH;
481     }

483     if (isGoHome == LOW && SetHomeX == HIGH) { // If Go Home Bu tton is
       Pressed
          digitalWrite(CalibrationLED1, LOW);
485       if (CurrentPosX > 0) {
                    MotorMove(1, HIGH, SpeedValue, CurrentPosX*ppmm);
487               }
                  else MotorMove(1, LOW, SpeedValue, abs(CurrentPosX)*ppmm);
489         CurrentPosX = 0;
        }
491   }

493   else if (isMotorSwitch_Y == LOW) { // If Y Motors are Selected
        if (isRotatePlus == LOW) { // If + Rotate Button is Pressed
495       MotorMove(2, LOW, SpeedValue, AngleValue*ppmm);
          CurrentPosY = CurrentPosY + AngleValue;
```

```
497     }
        else if (isRotateMinus == LOW) { // If - Rotate Button is Pressed
499       MotorMove(2, HIGH, SpeedValue, AngleValue*ppmm);
          CurrentPosY = CurrentPosY - AngleValue;
501     }
        else if (isSetHome == LOW && SetMode == HIGH) { // If Set Home Button
      is Pressed
503       digitalWrite(CalibrationLED2, HIGH);
          CurrentPosY = 0;
505       SetHomeY = HIGH;
        }
507
        if (isGoHome == LOW && SetHomeY == HIGH) { // If Go Home Button is
      Pressed
509       digitalWrite(CalibrationLED2, LOW);
          if (CurrentPosY > 0) {
511                 MotorMove(2, HIGH, SpeedValue, CurrentPosY*ppmm);
                  }
513               else MotorMove(2, LOW, SpeedValue, abs(CurrentPosY)*ppmm);
            CurrentPosY = 0;
515     }
      }
517 }
```

Immersion_Tank_Motor_Control.ino

Acronyms

AM Additive Manufacturing. 1

AMM Additively Manufactured Metal. 1

ANSI American National Standards Institute. 5

ASTM American Society of Testing and Materials. 8

DED Directed Energy Deposition. 1

EBM Electron Beam Melting. 1

ET Eddy Current Testing. 6

ISO International Organization for Standardization. 8

NDE Nondestructive Evaluation. 5

NIST National Institute of Standards and Technology. 8

PAUT Phased Array Ultrasonic Testing. 9

PBF Powder Bed Fusion. 1

PT Penetrant Testing. 6

RT Radiographic Testing. 6

SLM Selective Laser Melting. 1

UT Ultrasonic Testing. 7, 9

VT Visual Testing. 6

XCT X-ray Computed Tomography. 6

References

[1] I. Gibson, D. W. Rosen, and B. Stucker, *Additive Manufacturing Technologies: Rapid Prototyping to Direct Digital Manufacturing*. Springer, 2010.

[2] General Electric Additive, "GA-ASI Completes First Test Flight with Metal 3D-Printed Part," 2020.

[3] R. Wauthle, J. Van Der Stok, S. A. Yavari, J. Van Humbeeck, J. P. Kruth, A. A. Zadpoor, H. Weinans, M. Mulier, and J. Schrooten, "Additively Manufactured Porous Tantalum Implants," *Acta Biomaterialia*, vol. 14, pp. 217–225, 2015.

[4] D. Herzog, V. Seyda, E. Wycisk, and C. Emmelmann, "Additive Manufacturing of Metals," *Acta Materialia*, vol. 117, pp. 371–392, 2016.

[5] Manufacturing Guide, "Direct Laser Metal Sintering , DMLS."

[6] J. Evans, "DMLS: A Bumpy Road in History," 2014.

[7] W. Sames, F. Medina, W. Peter, S. Babu, and R. Dehoff, "Effect of Process Control and Powder Quality on Inconel 718 Produced Using Electron Beam Melting," in *8th International Symposium on Superalloy 718 and Derivatives*, 2014.

[8] C. Qiu, C. Panwisawas, M. Ward, H. C. Basoalto, J. W. Brooks, and M. M. Attallah, "On the Role of Melt Flow into the Surface Structure and Porosity Development During Selective Laser Melting," *Acta Materialia*, vol. 96, pp. 72–79, 2015.

[9] N. Hrabe, R. White, and E. Lucon, "Effects of Internal Porosity and Crystallographic Texture on Charpy Absorbed Energy of Electron Beam Melting Titanium Alloy (Ti-6Al-4V)," *Materials Science and Engineering A*, vol. 742, pp. 269–277, 2019.

[10] P. Edwards, A. O'Conner, and M. Ramulu, "Electron Beam Additive Manufacturing of Titanium Components: Properties and Performance," *Journal of Manufacturing Science*

and Engineering, *Transactions of the ASME*, vol. 135, no. 6, pp. 1–8, 2013.

[11] Q. C. Liu, J. Elambasseril, S. J. Sun, M. Leary, M. Brandt, and P. K. Sharp, "The Effect of Manufacturing Defects on the Fatigue Behaviour of Ti-6Al-4V Specimens Fabricated Using Selective Laser Melting," *Advanced Materials Research*, vol. 891-892, pp. 1519–1524, 2014.

[12] N. Kaufmann, M. Imran, T. M. Wischeropp, C. Emmelmann, S. Siddique, and F. Walther, "Influence of Process Parameters on the Quality of Aluminium Alloy EN AW 7075 Using Selective Laser Melting (SLM)," *Physics Procedia*, vol. 83, pp. 918–926, 2016.

[13] K. Kempen, L. Thijs, B. Vrancken, S. Buls, J. Van Humbeeck, and J. P. Kruth, "Producing Crack-Free, High Density M2 HSS Parts by Selective Laser Melting: Pre-Heating the Baseplate," in *24th International SFF Symposium - An Additive Manufacturing Conference, SFF 2013*, pp. 131–139, 2013.

[14] P. Mercelis and J. P. Kruth, "Residual Stresses in Selective Laser Sintering and Selective Laser Melting," *Rapid Prototyping Journal*, vol. 12, no. 5, pp. 254–265, 2006.

[15] N. T. Aboulkhair, N. M. Everitt, I. Ashcroft, and C. Tuck, "Reducing Porosity in AlSi10Mg Parts Processed by Selective Laser Melting," *Additive Manufacturing*, vol. 1, pp. 77–86, 2014.

[16] A. M. Mancisidor, F. Garciandia, M. S. Sebastian, P. Álvarez, J. Díaz, and I. Unanue, "Reduction of the Residual Porosity in Parts Manufactured by Selective Laser Melting Using Skywriting and High Focus Offset Strategies," *Physics Procedia*, vol. 83, pp. 864–873, 2016.

[17] R. Mertens, S. Dadbakhsh, J. Van Humbeeck, and J. P. Kruth, "Application of Base Plate Preheating During Selective Laser Melting," *Procedia CIRP*, vol. 74, pp. 5–11, 2018.

[18] J. Benzing, N. Hrabe, T. Quinn, R. White, R. Rentz, and M. Ahlfors, "Hot Isostatic Pressing (HIP) to Achieve Isotropic Microstructure and Retain As-Built Strength in an Additive Manufacturing Titanium Alloy (Ti-6Al-4V)," *Materials Letters*, vol. 257, 2019.

[19] S. Tammas-Williams, H. Zhao, F. Léonard, F. Derguti, I. Todd, and P. B. Prangnell, "XCT Analysis of the Influence of Melt Strategies on Defect Population in Ti-6Al-4V Components Manufactured by Selective Electron Beam Melting," *Materials Characterization*, vol. 102, pp. 47–61, 2015.

[20] J. M. Waller, B. H. Parker, K. L. Hodges, E. R. Burke, J. L. Walker, and E. R. Generazio, "Nondestructive Evaluation of Additive Manufacturing State-of-the-Discipline Report," tech. rep., National Aeronautics and Space Agency, 2014.

[21] America Makes and ANSI Additive Manufacturing Standardization Collaborative, "Standardization Roadmap for Additive Manufacturing - Version 2.0," tech. rep., 2018.

[22] H. Speckman, "NDT Challenges and Solutions for Metal Additive Manufactured (AM) Parts and Structures," in *Space Tech Expo, Bremen, Germany*, 2017.

[23] J. C. Fox, F. Kim, Z. Reese, and C. Evans, "Complementary Use of Optical Metrology and X-Ray Computed Tomography for Surface Finish and Defect Detection in Laser Powder Bed Fusion Additive Manufacturing," in *Proceedings - 2018 ASPE and euspen Summer Topical Meeting: Advancing Precision in Additive Manufacturing*, pp. 195–200, 2018.

[24] F. H. Kim, S. P. Moylan, and E. J. Garboczi, "Preparation of Cylindrical Tensile Specimens for Simultaneous Mechanical Testing and X-ray Computed Tomography," tech. rep., National Institute of Standards and Technology, 2019.

[25] J. Kastner and C. Heinzel, "X-ray Computed Tomography for Non-destructive Testing and Materials Characterization," in *Integrated Imaging and Vision Techniques for Industrial Inspection: Advances and Applications*, pp. 227–250, 2015.

[26] L. W. Koester, L. J. Bond, H. Taheri, and P. C. Collins, "Nondestructive Evaluation of Additively Manufactured Metallic Parts: In Situ and Post Deposition," in *Additive Manufacturing for the Aerospace Industry*, pp. 401–417, Elsevier Inc., 2019.

[27] Energetics Incorporated, "Measurement Science Roadmap for Metal-Based Additive Manufacturing," tech. rep., National Institute of Standards and Technology, 2013.

[28] "ASTM F3122-14, Standard Guide for Evaluating Mechanical Properties of Metal Materials Made via Additive Manufacturing Processes," 2014.

[29] "ISO / ASTM52907-19, Additive Manufacturing — Feedstock Materials — Methods to Characterize Metallic Powders," 2019.

[30] "ISO/ASTM AWI 52909 (Under Development), Additive Manufacturing — Finished Part Properties — Orientation and Location Dependence of Mechanical Properties for Metal Powder Bed Fusion," 2018.

[31] "ASTM WK69731 (Under Development), New Guide for Additive Manufacturing – Non-Destructive Testing (NDT) for Use in Directed Energy Deposition (DED) Additive Manufacturing Processes," 2019.

[32] "ASTM E3166-20e1, Standard Guide for Nondestructive Examination of Metal Additively Manufactured Aerospace Parts After Build," 2020.

[33] "ISO/ASTM CD TR 52906 (Under Development), Additive Manufacturing — Non-Destructive Testing and Evaluation — Standard Guideline for Intentionally Seeding Flaws in Parts," 2018.

[34] "ISO/ASTM DTR 52905 (Under Development), Additive Manufacturing — General Principles — Non-Destructive Testing of Additive Manufactured Products," 2016.

[35] R. Russell, D. Wells, J. Waller, B. Poorganji, E. Ott, T. Nakagawa, H. Sandoval, N. Shamsaei, and M. Seifi, "Qualification and Certification of Metal Additive Manufactured Hardware for Aerospace Applications," in *Additive Manufacturing for the Aerospace Industry*, pp. 33–66, Elsevier Inc., 2019.

[36] NDT Resource Center, "Basic Principles of Ultrasonic Testing."

[37] The American Society for Nondestructive Testing, *Materials and Processes for NDT Technology*. 2 ed., 2016.

[38] TecScan, "Ultrasonic C-Scan Imaging for Evaluating the Integrity of Brazed Parts Ultrasonic C-Scan for Braze Bond Testing," 2015.

[39] J. Prasad and C. G. Krishnadas Nair, "Ultrasonics," in *Non-Destructive Test and Evaluation of Materials*, p. 86, McGraw-Hill, 2 ed., 2011.

[40] T. DebRoy, H. L. Wei, J. S. Zuback, T. Mukherjee, J. W. Elmer, J. O. Milewski, A. M. Beese, A. Wilson-Heid, A. De, and W. Zhang, "Additive Manufacturing of Metallic Components – Process, Structure and Properties," *Progress in Materials Science*, vol. 92, pp. 112–224, 2018.

[41] T. Sol, S. Hayun, D. Noiman, E. Tiferet, O. Yeheskel, and O. Tevet, "Nondestructive Ultrasonic Evaluation of Additively Manufactured AlSi10Mg Samples," *Additive Manufacturing*, vol. 22, pp. 700–707, aug 2018.

[42] Y. Song, X. Zi, Y. Fu, X. Li, C. Chen, and K. Zhou, "Nondestructive Testing of Additively Manufactured Material Based on Ultrasonic Scattering Measurement," *Measurement*, vol. 118, pp. 105–112, 2018.

[43] N. V. Karthik, H. Gu, D. Pal, T. Starr, and B. Stucker, "High Frequency Ultrasonic Non Destructive Evaluation of Additively Manufactured Components," in *24th International SFF Symposium - An Additive Manufacturing Conference, SFF 2013*, pp. 311–325, 2013.

[44] Z. Zhou, W. Li, Y. Li, and S. Li, "Research on Ultrasonic Array Testing Method for Additive-Manufactured Titanium Alloy," in *International Symposium on Structural Health Monitoring and Nondestructive Testing*, 2018.

[45] Z. Prevorovsky, J. Krofta, and J. Kober, "NDT in Additive Manufacturing of Metals," in *IXth NDT in Progress*, pp. 75–84, 2017.

[46] H. Jeong, "Focusing a Flexible Ultrasonic Array Transducer Using a Time Reversal Technique for Discontinuities Within Complex Geometries," *Materials Evaluation*, vol. 70, no. 2, pp. 173–179, 2012.

[47] H. Jeong, "Time Reversal-Based Beam Focusing of an Ultrasonic Phased Array Transducer on a Target in Anisotropic and Inhomogeneous Welds," *Materials Evaluation*, vol. 72, no. 5, pp. 589–596, 2014.

[48] A. B. Lopez, J. Santos, J. P. Sousa, T. G. Santos, and L. Quintino, "Phased Array Ultrasonic Inspection of Metal Additive Manufacturing Parts," *Journal of Nondestructive Evaluation*, vol. 38, 2019.

[49] H. Rieder, A. Dillhöfer, M. Spies, J. Bamberg, and T. Hess, "Online Monitoring of Additive Manufacturing Processes Using Ultrasound," in *Proceedings of the 11th European Conference on Non-Destructive Testing*, vol. 1, 2014.

[50] M. Souissi, *Using Helical Lamb Ultrasonic Waves for Tomography and Delamination Detection of Cylindrical Objects*. PhD thesis, University of New Haven, 2019.

[51] F. H. Hotchkiss, "Guide to Designs of IIW-Type Blocks," *NDT International*, vol. 23, no. 6, pp. 319–331, 1990.

[52] L. Thijs, F. Verhaeghe, T. Craeghs, J. V. Humbeeck, and J. P. Kruth, "A Study of the Microstructural Evolution During Selective Laser Melting of Ti-6Al-4V," *Acta Materialia*, vol. 58, no. 9, pp. 3303–3312, 2010.

[53] O. Yeheskel and O. Tevet, "Elastic Moduli of Transparent Yttria," *Journal of the American Ceramic Society*, vol. 82, no. 1, pp. 136–144, 1999.

[54] C. Hellier, "Ultrasonic Testing," in *Handbook of Nondestructive Evaluation*, ch. 7, pp. 7.10–7.11, McGraw-Hill, 2 ed., 2013.

[55] J. L. Rose, *Ultrasonic Guided Waves in Solid Media*. Cambridge University Press, 2014.

[56] MatWeb Material Property Data, "AK Steel 316L Austenitic Stainless Steel."

[57] A. Nandy, S. Mullick, and D. Datta, "Numerical Simulation of Ultrasonic Wave Propagation in Flawed Domain," in *Proceedings of the National Seminar & Exhibition on Non-Destructive Evaluation*, pp. 160–163, 2009.

[58] A. Van Pamel, P. Huthwaite, C. R. Brett, and M. J. Lowe, "Numerical Simulations of Ultrasonic Array Imaging of Highly Scattering Materials," *NDT&E International*, vol. 81, pp. 9–19, 2016.

[59] C. A. Leckey, K. R. Wheeler, V. N. Hafiychuk, H. Hafiychuk, and D. A. Timuçin, "Simulation of Guided-Wave Ultrasound Propagation in Composite Laminates: Benchmark Comparisons of Numerical Codes and Experiment," *Ultrasonics*, vol. 84, pp. 187–200, 2018.

[60] S. Raley and E. A. Dieckman, *Application of Elastodynamic Finite Integration Technique (EFIT) to Three-Dimensional Wave Propagation and Scattering in Arbitrary Geometries*. PhD thesis, University of New Haven, 2019.